

AD A122608

# NAVAL POSTGRADUATE SCHOOL

Monterey, California



## THESIS

THERMAL COUPLING AND DAMAGE MECHANISMS OF  
1.06 MICRON LASER RADIATION AND LASER-  
PRODUCED PLASMA ON SELECTED MATERIALS

by

William Frost Jenkins

and

William Richard Schmidt

December 1968

Thesis Advisor

J. K. Schwynke

TOP SECRET COPY

**Best  
Available  
Copy**



Unclassified

SECURITY CLASSIFICATION OF THIS PAGE/When Data Entered

Item 20. (continued)

polished, unpolished, and Si-coated surface preparations, as well as TiC-coated stainless steel. The experiments were conducted in a  $10^{-6}$  torr, vacuum using a neodymium-glass laser in the Q-switched mode.

For uncoated targets a direct correlation exists between thermal coupling and the percent of irradiated surface experiencing breakdown. For coated targets, thermal coupling is dependent on coating thickness and smoothness. Silicon and TiC-coated targets are found to experience unipolar arcing damage. A model is proposed to describe the relationship between arc crater and target properties.



A

DD Form 1473  
Jan 73  
S/N 0102-014-6601

112  
Unclassified

SECURITY CLASSIFICATION OF THIS PAGE/When Data Entered

Approved for public release; distribution unlimited

Thermal Coupling and Damage Mechanisms of 1.06 Micron Laser  
Radiation and Laser-Produced Plasma on Selected Materials

by

William Frost Jenkins  
Lieutenant Commander, United States Navy  
B.S., United States Naval Academy, 1970

and

William Richard Schmidt  
Lieutenant Commander, United States Navy  
B.S., United States Naval Academy, 1970

Submitted in partial fulfillment of the  
requirements for the degree of

MASTER OF SCIENCE IN PHYSICS

from the

NAVAL POSTGRADUATE SCHOOL

December 1982

Author:

William Frost Jenkins

Author:

William Richard Schmidt

Approved by:

Fred R. Schuurbe

Thesis Advisor

Kenneth D. Challen

Second Reader

W. Dyer

Chairman, Department of Physics

William M. Tolles

Dean of Science and Engineering

## ABSTRACT

Thermal coupling and plasma-induced surface damage were investigated for selected target materials to determine the correlation between the two phenomena. A review of thermal coupling and unipolar arcing, along with reference to the physical properties of the target materials involved, provided the basis on which this study was conducted. Target materials investigated included aluminum and stainless steel, both with polished, unpolished, and Si-coated surface preparations, as well as TiC-coated stainless steel. The experiments were conducted in a  $10^{-6}$  torr. vacuum using a neodymium-glass laser in the Q-switched mode.

For uncoated targets, a direct correlation exists between thermal coupling and the percent of irradiated surface experiencing breakdown. For coated targets, thermal coupling is dependent on coating thickness and smoothness. Silicon and TiC-coated targets are found to experience unipolar arcing damage. A model is proposed to describe the relationship between arc crater size and target properties.

TABLE OF CONTENTS

I.	INTRODUCTION	16
II.	BACKGROUND AND THEORY	18
	A. INTRODUCTION	18
	B. COUPLING OF ENERGY TO A METAL TARGET	20
	1. Loss Mechanisms	20
	2. Absorption of Energy	22
	3. Thermal Coupling	28
	a. Skin Depth	28
	b. Heat Conduction and Thermal Diffusivity	28
	c. Thermal Coupling Coefficient	31
	C. PLASMA-SURFACE INTERACTIONS	34
	1. Sheath Effects	34
	2. Unipolar Arcing	35
	3. Discussion	38
III.	EXPERIMENTAL DESIGN	40
	A. EQUIPMENT	40
	1. Laser System	40
	2. Target Test Chamber	42
	3. Thermal Data Recording	42
	4. Scanning Electron Microscope	44
	5. CW Laser System	44

B.	PROCEDURE .....	44
1.	Plasma Onset .....	44
2.	Thermal Coupling .....	45
3.	Surface Damage .....	45
4.	Target Specular Reflectivity .....	46
5.	Sample Preparations .....	46
IV.	EXPERIMENTAL RESULTS .....	50
A.	PLASMA ONSET .....	50
1.	TiC-Coated SS-304 Foil .....	50
2.	Unpolished 2024 Aluminum .....	50
3.	Polished 2024 Aluminum .....	51
4.	Polished 2024 Aluminum Coated with 0.2 Micron Silicon .....	51
5.	Polished 2024 Aluminum Coated with 1 Micron Silicon .....	51
B.	THERMAL COUPLING .....	52
1.	2024 Aluminum .....	52
a.	Unpolished aluminum .....	52
b.	Polished aluminum .....	53
c.	Polished aluminum coated with 0.2 micron silicon .....	53
d.	Polished aluminum coated with 1 micron silicon .....	53
2.	SS-304 .....	54
a.	Unpolished SS-304 .....	54
b.	Polished SS-304 .....	54
c.	Polished SS-304 coated with silicon .....	55

C.	SURFACE DAMAGE AND UNIPOLAR ARCING -----	55
1.	Aluminum Targets at Plasma Onset -----	55
a.	Unpolished 2024 Aluminum -----	55
b.	Polished 2024 Aluminum -----	57
2.	Silicon-coated Aluminum at Plasma Onset ----	57
a.	0.2 Micron Silicon Coat on Polished Aluminum -----	57
b.	1 Micron Silicon Coat on Polished Polished Aluminum -----	60
3.	TiC-Coated SS-304 at Plasma Onset -----	60
4.	Aluminum Targets at $10^8$ W/cm <sup>2</sup> -----	60
a.	Unpolished 2024 Aluminum -----	60
b.	Polished 2024 Aluminum -----	63
5.	Silicon-Coated Aluminum at $10^8$ W/cm <sup>2</sup> -----	63
a.	0.2 Micron Silicon Coat -----	63
b.	1 Micron Silicon Coat -----	66
6.	SS-304 at $10^8$ W/cm <sup>2</sup> -----	66
a.	Unpolished SS-304 -----	66
b.	Polished SS-304 -----	69
c.	TiC-coated SS-304 -----	69
d.	1-2 Micron Silicon Coat on SS-304 -----	74
D.	SAMPLE SPECULAR REFLECTIVITY -----	77
V.	DISCUSSION OF RESULTS -----	78
A.	PLASMA ONSET -----	78
B.	THERMAL COUPLING -----	81
1.	2024 Aluminum -----	81

2.	SS-304 -----	85
3.	Experimental Limitations -----	86
C.	SURFACE DAMAGE EFFECTS -----	86
1.	2024 Aluminum -----	86
2.	SS-304 -----	87
3.	Silicon Coatings -----	88
4.	TiC Coating -----	92
5.	Crater Size -----	95
D.	SPECULAR REFLECTIVITY -----	98
VI.	SUMMARY AND CONCLUSIONS -----	101
VII.	RECOMMENDATIONS -----	105
	APPENDIX A: PHYSICAL PROPERTIES OF SELECTED MATERIALS --	107
	APPENDIX B: TABLES -----	108
	LIST OF REFERENCES -----	122
	INITIAL DISTRIBUTION LIST -----	125

LIST OF TABLES

1.	Time to Reach Boiling Temperature for Target Material -----	108
2.	Skin Depth for Target Material -----	109
3.	Diffusivity Times for Target Material -----	109
4.	Plasma Onset Data for TiC-coated SS-304 Foil -----	110
5.	Plasma Onset Data for Unpolished 2024 Aluminum -----	111
6.	Plasma Onset Data for Polished 2024 Aluminum -----	112
7.	Plasma Onset Data for 0.2 Micron Si Coating on Polished 2024 Aluminum -----	114
8.	Plasma Onset Data for 1 Micron Si Coating on Polished 2024 Aluminum -----	114
9.	Thermal Coupling Data for Unpolished 2024 Aluminum--	115
10.	Thermal Coupling Data for Polished 2024 Aluminum ---	116
11.	Thermal Coupling Data for 0.2 Micron Si Coating on Polished 2024 Aluminum -----	117
12.	Thermal Coupling Data for 1 Micron Si Coating on Polished 2024 Aluminum -----	117
13.	Thermal Coupling Data for Unpolished 304 Stainless Steel -----	118
14.	Thermal Coupling Data for Polished 304 Stainless Steel -----	119
15.	Thermal Coupling Data for Si Coating on Polished 304 Stainless Steel -----	119
16.	Summary of TiC Surface Damage Evaluation Shots -----	120
17.	Measured Sample Specular Reflectivities -----	121

LIST OF FIGURES

1.	Power Balance Diagram for Laser-Surface Interaction -----	19
2.	Reflectance as a Function of Time for Aluminum ----	21
3.	Reflectivity as a Function of Time for Stainless Steel -----	21
4.	Reflectivity as a Function of Irradiance for Aluminum -----	23
5.	Schematic Representation of the Depth Vaporized in a Metallic Target as a Function of Time -----	25
6.	Pressure Dependence of Thermal Coupling for Aluminum -----	32
7.	Thermal Coupling Coefficient of Aluminum at 1.06 Microns as a Function of Incident Power Density ---	32
8.	Unipolar Arc Model -----	37
9.	Schematic of Pulsed Laser and Test Chamber Arrangement -----	41
10.	Aluminum Vacuum Chamber Diagram, Top View -----	43
11.	Schematic of Equipment Arrangement for Specular Reflectivity Measurement -----	47
12.	Unpolished 2024 Aluminum Before Irradiation, SEM 1200X -----	56
13.	Unpolished 2024 Aluminum After Irradiation with 4 MW/cm <sup>2</sup> Plasma Onset Power Density, SEM 1100X ---	56
14.	Polished 2024 Aluminum Before Irradiation, SEM 5000X -----	58
15.	Polished 2024 Aluminum After Irradiation with 18 MW/cm <sup>2</sup> Plasma Onset Power Density, SEM 5000X -----	58
16.	0.2 Micron Silicon Coating Over Polished 2024 Aluminum Before Irradiation, SEM 5000X -----	59

17.	0.2 Micron Silicon Coating Over Polished 2024 Aluminum After Irradiation with 7.4 MW/cm <sup>2</sup> Plasma Onset Power Density, SEM 5000X -----	59
18.	1 Micron Silicon Coating Over Polished 2024 Aluminum Before Irradiation, SEM 5000X -----	61
19.	1 Micron Silicon Coating Over Polished 2024 Aluminum After Irradiation with 9.8 MW/cm <sup>2</sup> Plasma Onset Power Density, Edge of Damage Area, SEM 5800X -----	61
20.	1 Micron Silicon Coating Over Polished 2024 Aluminum After Irradiation with 9.8 MW/cm <sup>2</sup> Plasma Onset Power Density, a Flaked Area, SEM 5800X -----	62
21.	TiC Coating Over SS-304 Before Irradiation, SEM 490X -----	62
22.	Unpolished 2024 Aluminum After Irradiation with 400 MW/cm <sup>2</sup> , Edge of Damage Spot, SEM 550X -----	64
23.	Large Crater in Unmelted Region of Unpolished 2024 Aluminum Target, SEM 5500X -----	64
24.	Polished 2024 Aluminum After Irradiation with 400 MW/cm <sup>2</sup> , Typical Melted and Arced Area, SEM 475X -----	65
25.	Polished 2024 Aluminum After Irradiation With 400 MW/cm <sup>2</sup> , Edge of Melted Area, Typical Arcing Over Unmelted Surface, SEM 460X -----	65
26.	0.2 Micron Silicon Coating Over Polished 2024 Aluminum After Irradiation with 400 MW/cm <sup>2</sup> After Etching Edge of Damage Area, SEM 10,800X -----	67
27.	1 Micron Silicon Coating Over Polished 2024 Aluminum After Irradiation with 400 MW/cm <sup>2</sup> Center of Damage Area, SEM 1150X -----	67
28.	1 Micron Silicon Coating Over Polished 2024 Aluminum After Irradiation with 400 MW/cm <sup>2</sup> Near Edge of Irradiated Area, SEM 5600X -----	68
29.	1 Micron Silicon Coating Over Polished 2024 Aluminum After Irradiation with 400 MW/cm <sup>2</sup> , Outside Edge of Irradiated Area, SEM 21,500X -----	68
30.	Unpolished SS-304 After Irradiation with 400 MW/cm <sup>2</sup> , SEM 235X -----	70

31.	Unpolished SS-304 After Irradiation with 400 MW/cm <sup>2</sup> , SEM 2350X -----	70
32.	Polished SS-304 After Irradiation with 400 MW/cm <sup>2</sup> , SEM 230X -----	71
33.	Polished SS-304 After Irradiation with 400 MW/cm <sup>2</sup> , SEM 1150X -----	71
34.	TiC Coated SS-304 After Irradiation with 300 MW/cm <sup>2</sup> , SEM 4800X -----	72
35.	TiC Coated SS-304 After Irradiation with 872 MW/cm <sup>2</sup> , SEM 1200X -----	72
36.	TiC Coated SS-304 After Irradiation with 1096 MW/cm <sup>2</sup> , SEM 5,400X -----	73
37.	1-2 Micron Silicon Coating Over SS-304 Before Irradiation, SEM 2100X -----	73
38.	1-2 Micron Silicon Coating Over SS-304 After Irradiation with 400 MW/cm <sup>2</sup> , Edge of Damage Area, SEM 2330X -----	75
39.	1-2 Micron Silicon Coating Over SS-304 After Irradiation with 400 MW/cm <sup>2</sup> , Near Edge of Irradiated Area, SEM 2380X -----	75
40.	1-2 Micron Silicon Coating Over SS-304 After Irradiation with 400 MW/cm <sup>2</sup> , Site of Greatest Apparent Melting, SEM 2300X -----	76
41.	1-2 Micron Silicon Coating Over SS-304 After Irradiation with 400 MW/cm <sup>2</sup> , Spheroid Formation Around Holes in Coating, SEM 5500X -----	76
42.	TiC Coated SS-304 Irradiated with 75 MW/cm <sup>2</sup> , Streaks Caused by Coating Blowing off Normal to Target Surface -----	94

TABLE OF SYMBOLS

<u>Symbol</u>	<u>Quantity</u>	<u>Units Used</u>
K	Thermal Conductivity	W/cm-K
$\rho$	Density	g/cm <sup>3</sup>
c	Specific Heat	J/g-K
P <sub>D</sub>	Absorbed Laser Power Density	W/cm <sup>2</sup>
T <sub>B</sub>	Boiling Temperature	K
T <sub>O</sub>	Ambient Temperature	K
$\omega_p$	Plasma Frequency	Rad/Sec
e	Unit of Charge	1.6 x 10 <sup>-19</sup> C (MKS) 4.8 x 10 <sup>-10</sup> Statcoul (CGS)
n	Electron Density	m <sup>-3</sup> (MKS) cm <sup>-3</sup> (CGS)
m	Electron Rest Mass	9.11 x 10 <sup>-31</sup> Kg (MKS) 9.11 x 10 <sup>-28</sup> g (CGS)
$\delta$	Skin Depth	m
$\sigma$	Electrical Conductivity	mho/m
$\mu$	Magnetic Permeability	Henries/m
$\mu_0$	Magnetic Permeability of Vacuum	1.2566 x 10 <sup>-6</sup> H/m
$\nu$	Frequency	sec <sup>-1</sup>
$\kappa$	Thermal Diffusivity	cm <sup>2</sup> /sec
Q	Heat Production/Unit Volume/ Unit Time	W/cm <sup>3</sup>
d	Target Thickness	cm

<u>Symbol</u>	<u>Quantity</u>	<u>Units Used</u>
$\tau_d$	Axial Thermal Diffusion Time	sec
$r_o$	Laser Focal Spot Size	cm
$\tau_r$	Radial Thermal Diffusion Time	sec
$\alpha$	Thermal Coupling Coefficient	Dimensionless
$\Delta T$	Maximum Observed Temperature Rise on Target Back Surface	K
$E_D$	Energy Density Incident on Target	J/cm <sup>2</sup>
$E_T$	Energy Incident on Target	J
$V_f$	Plasma Sheath Potential	Statvolt
$KT_e$	Electron Thermal Energy	Ergs
$M_i$	Ion Rest Mass	g
$\lambda_D$	Debye Length	cm
$P_R$	Ohmic Power	Watts
$I$	Current	Amps
$R$	Resistance	Ohms
$j(r)$	Crater Radial Current Density	A/m <sup>2</sup>
$\Delta Z$	Crater Depth	m
$r$	Crater Radius	m
$\gamma$	Resistivity	Ohm-m
$V$	Crater Volume	m <sup>3</sup>
$j_s$	Crater Surface Current Density	A/m <sup>2</sup>

## ACKNOWLEDGEMENT

We wish to thank Professors F. Schwirzke and K. D. Challenger for their help, guidance, and encouragement throughout this thesis. We would also like to express our gratitude to Robert Sanders for his help in the Plasma Physics Lab, and Thomas Kellogg for his assistance and guidance in the sample preparation room and with the SEM.

## I. INTRODUCTION

The interactions of a laser-produced plasma with various surfaces is receiving intense research from many disciplines. The possible use of high energy lasers in weapons applications makes the understanding of the interactions important for both shielding and weapons design requirements. Material interaction with laser radiation affects the thickness of the surface involved in plasma formation, while interaction with the plasma determines the portion of total energy coupled to the material.

Unipolar arcing has been shown to be a significant plasma-surface interaction with serious implications for magnetic confinement fusion devices. The process has been studied extensively at the Naval Postgraduate School, with particular attention being given to the Schwirzke-Taylor model. Keville and Lautrop [Ref. 1] initially studied arcing from a laser-produced plasma and found that TiC coatings were very arc resistant. Barker and Rush, Ryan and Shedd, and Hoover [Refs. 2-4] all studied plasma-surface interactions and arcing over conductors, semi-conductors, insulators, and metallic glasses to verify present models, and to locate arc-resistant materials. Beelby and Ulrich [Ref. 5] investigated plasma onset and arc initiation in various materials and the mechanisms of onset. Metheny [Ref. 6]

studied thermal and momentum coupling to various arc-resistant and arc-susceptible conductors.

The study reported here dealt with thermal coupling of energy from the laser-produced plasma to the surface of various materials, and with arcing and other surface damage mechanisms. The thermal coupling experiments were conducted using AISI 304 stainless steel, AISI 2024 aluminum, and thin silicon coatings on SS-304 and Al-2024. Surface damage effects and arcing were examined for all the above materials as well as thin TiC films on SS-304. A neodymium-glass laser as operated in the Q-switched mode and fired through neutral-density filters into a vacuum chamber containing the targets. Thermal energy was measured using a thermocouple placed at the back of each target to measure the temperature increase after irradiation. A scanning electron microscope was used to examine surface damage to the targets in detail.

## II. BACKGROUND AND THEORY

### A. INTRODUCTION

The field of study which encompasses laser-surface interactions is one which has received considerable attention over the past two decades. Two of the primary areas of concern include coupling of laser energy to a target, with application to laser weapons systems, and plasma-surface interaction which occurs after a laser has produced a plasma, with application to controlled nuclear fusion programs as well as laser weapons systems. In discussing laser-surface interactions, one must keep in mind the complex nature of the coupling and loss processes involved. Figure 1 presents a sequence of events and their feedback mechanisms in a logical sequence. The scheme represented in this figure is useful from a welding point of view, and does not account for plasma-surface interactions which are of concern in tokamaks.

When laser energy is incident on a target, the plasma created may cause damage by thermal and mechanical processes, such as sputtering, blistering, and vaporization. Additionally, an electrical process, referred to as unipolar arcing, leads to crater formation, which is a well-known damage mechanism which introduces high-Z elemental impurities in tokamaks. Unipolar arcing may also be a major damage mechanism to be considered in destruction of targets by laser weapons. The

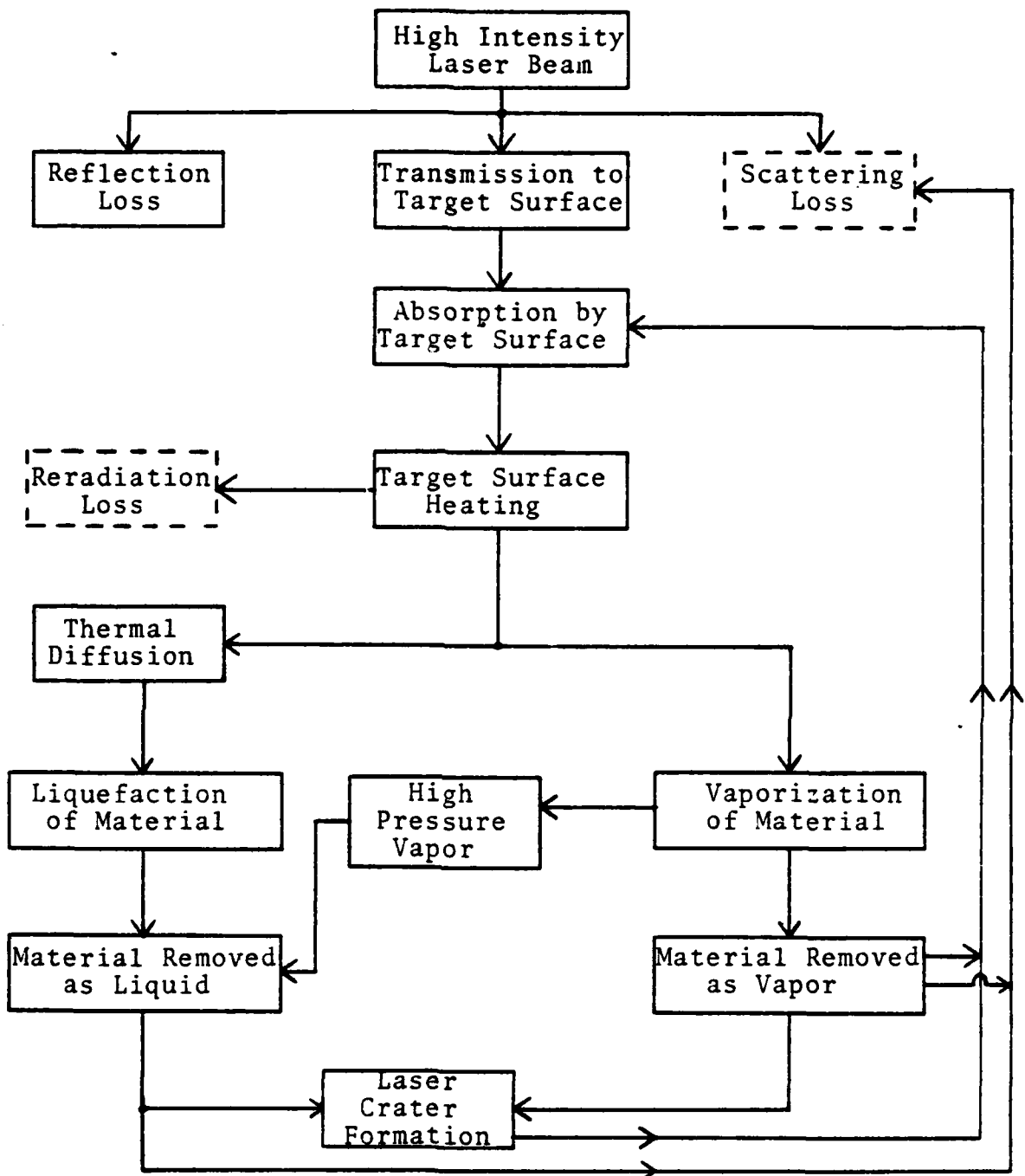


Figure 1. Power Balance Diagram for Laser-Surface Interaction. [from Ref. 7]. Dotted boxes are negligible for short pulse length laser. This scheme neglects plasma-surface interaction phenomena.

laser beam parameters, including energy density, pulse duration, and wavelength, have a direct effect in determining which damage and loss mechanisms will be important.

## B. COUPLING OF ENERGY TO A METAL TARGET

### 1. Loss Mechanisms

Laser energy incident on a surface will experience scattering and reflection losses, reducing the absorption of energy. Laser beam blocking due to scattering by ejected material can be considered negligible for short pulse duration lasers [Ref. 7]. Therefore, for an opaque target, absorptivity can be expressed as  $A=1-R$ , where  $R$  is the reflectivity. Reflectivity is defined as the ratio of the power reflected from the target to the power incident on the target. Thus a decrease in reflectivity leads to enhanced coupling of energy to the surface.

Metals in general have high reflectivity values. Aluminum, for example, has a reflectivity of about 80% at 1.06 micron radiation, which is the wavelength of the Nd:glass laser used in this thesis. Additionally, most metals exhibit an increase in reflectivity with an increase in wavelength of the illuminating source [Ref. 8: p. 341].

There is strong evidence that reflectivity decreases during a laser pulse. Figures 2 and 3 show sharp drops in reflectivity for short illumination times, but after a sufficient period of time the reflectivity remains essentially

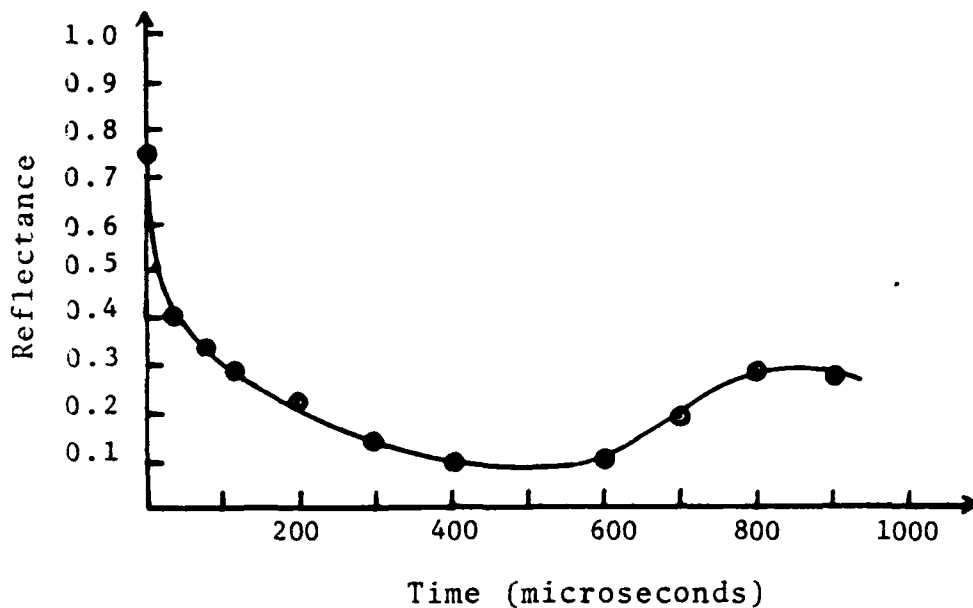


Figure 2. Reflectance as a Function of Time for Aluminum. Each measurement was made during a single laser pulse, using a Nd-YAG laser (1.06 micron), 30 KW average power,  $10^7$  W/cm<sup>2</sup> power density [Ref. 7]. Reflectance as used in this reference is synonymous with reflectivity.

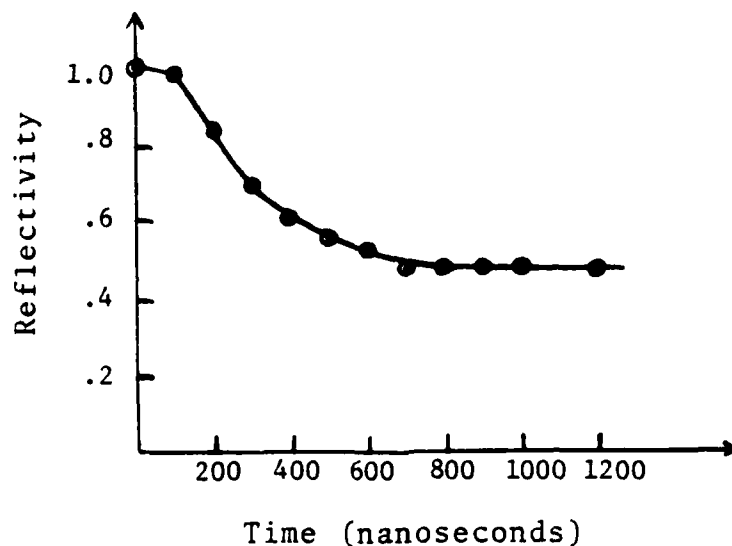


Figure 3. Reflectivity as a Function of Time for Stainless Steel. A CO<sub>2</sub> TEA laser (10.6 micron) was used with a  $1.5 \times 10^8$  W/cm<sup>2</sup> power density [Ref. 8: p. 343].

constant. This leveling out of reflectivity at longer times is accounted for by reduced absorption as the vaporization temperature of the metal is reached [Ref. 7].

Reflectivity also varies inversely with increasing irradiance, as depicted in Figure 4. From Figures 2 through 4 it is clear that an increase in temperature of the metal surface, due to longer illumination times or increased irradiance levels, leads to a reduction in reflectivity and an increase in absorptivity. Energy is more effectively coupled to a surface as the surface temperature increases up to a point determined by plasma characteristics.

## 2. Absorption of Energy

The percent of incident laser energy that is absorbed by a target will rapidly heat the surface. As discussed above, absorption increases with temperature. The intense laser radiation will cause liquefaction and vaporization of the target material. The amount of material vaporized as opposed to that liquefied is dependent on the laser power density. For densities on the order of  $10^6 - 10^8$  W/cm<sup>2</sup>, vaporization is the dominant process [Ref. 8].

Early in the laser pulse, the surface material begins to vaporize. The time in seconds to vaporize, i.e., to reach the boiling temperature, is given [Ref. 8: p. 344] by

$$t_B = \left(\frac{\pi}{4}\right) \left(\frac{K_0 c}{P_D}\right) (T_B - T_0)^2. \quad (1)$$

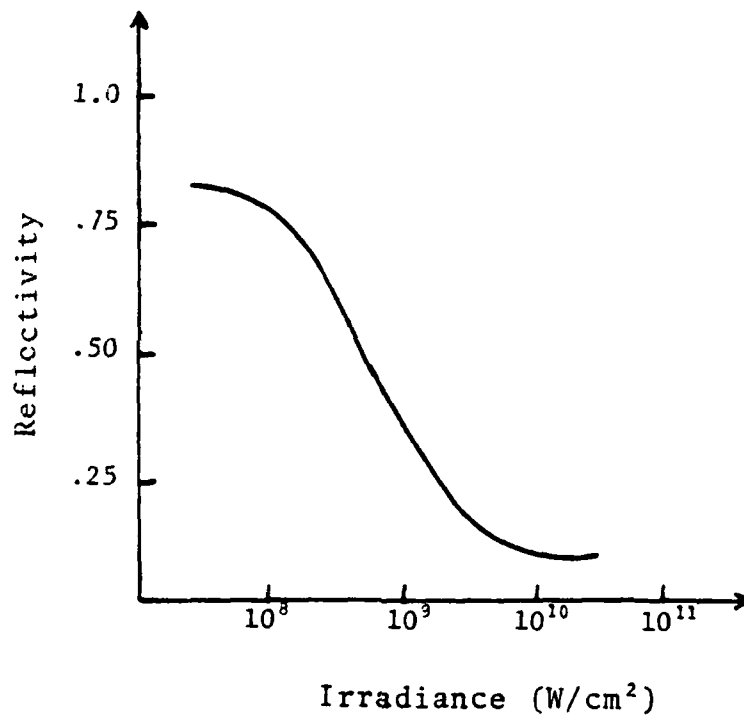


Figure 4. Reflectivity as a Function of Irradiance for Aluminum. The plot is for a Q-switched laser pulse of 15 nsec duration [Ref. 15: p. 116].

Using values from Appendix A and a power density of 400 MW/cm<sup>2</sup>, which is a typical value for power densities used in this thesis, vaporization times for the four target materials used in this study are listed in Table 1. Calculations assume that all incident laser power is absorbed. A 20 nanosecond FWHM Q-switched laser pulse was used in the investigations of this thesis. Thus, it is apparent that the surface material begins to vaporize very early in the laser pulse.

In the higher power density regime, in excess of 10<sup>7</sup> W/cm<sup>2</sup>, the vaporized material ionizes and becomes an optically dense, high temperature plasma. The laser light is effectively cut off from the target surface. However, the plasma is highly absorbing, as determined by its density and temperature profiles, and is able to convert optical energy to thermal energy. The thermal energy is then transmitted to the target surface by means of reradiation at shorter wavelengths (ultraviolet) or by electron conduction [Ref. 9]. The opacity of the plasma dominates the absorption process for the majority of the laser pulse length, as depicted in Figure 5. It is in this power regime that a plasma is able to transfer thermal energy more efficiently to the target than if the optical energy were impinging directly on the target [Ref. 10]. This plasma-efficient energy transfer is referred to as enhanced coupling and will be discussed in the next section (Thermal Coupling).

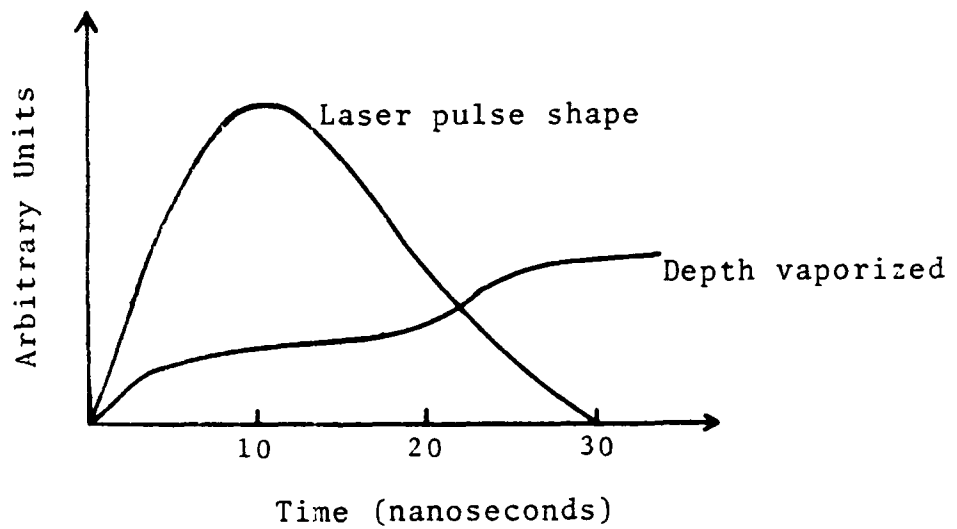


Figure 5. Schematic Representation of the Depth Vaporized in a Metallic Target as a Function of Time. [Ref. 15: p. 112].

If laser power density exceeds a value on the order of  $10^8$  W/cm<sup>2</sup>, the opaque plasma will propagate toward the lasing source and incident energy will be decoupled from the target. This phenomenon is referred to as a laser-supported absorption (LSA) wave, and is treated in detail in a report by Harrison and Neighbors [Ref. 11]. Any further increase in power density leads to an increase in the speed of propagation of the LSA Wave away from the target, leading to a greater decoupling of energy from the target [Refs. 9, 12]. The LSA wave phenomenon is essentially an atmospheric process. For targets in a near vacuum, the LSA wave will no longer be able to propagate. However, Hettche et al [Ref. 9] found no consistent differences in thermal coupling for targets in air and vacuum, suggesting that even in a vacuum, enough target material is vaporized in front of the target to decouple incident energy from the target.

If the laser beam is of sufficient length or power, the plasma density will increase, leading to an increase in the plasma frequency  $\omega_p$  [Ref. 13: p. 73], where, using CGS units,

$$\omega_p = \left( \frac{4 \pi n e^2}{m} \right)^{1/2}$$

When the density is greater than a critical value  $n_c$ , the plasma frequency exceeds the incident frequency and waves can no longer propagate in the plasma. This condition is called plasma cutoff [Ref. 13: p. 103]. For incident 1.06

micron laser radiation, the critical density is about  $10^{21}$   $\text{cm}^{-3}$ , which is quite high. When cutoff is reached, the plasma becomes opaque and reflects energy incident on it. However, plasma expansion occurs on the order of  $10^7$  cm/sec in the normal and radial directions, reducing the plasma density [Ref. 14]. Thus the laser-plasma interaction process is a dynamic one which may or may not include cutoff, but which certainly includes plasma absorption of energy and the retransmission of that energy to the target surface.

Referring again to Figure 5, it is apparent that late in the laser pulse, incident laser energy is once again being reradiated by the plasma to the surface and vaporization is occurring [Ref. 15].

Energy coupling to a target is a complex process that depends not only on the target characteristics and laser beam parameters, but also on the dynamics of the expanding plasma. The energy coupling to the target, in turn, determines the scope of damage that will be incurred.

In order to more fully understand and appreciate energy coupling to a target, several types of coupling measurements may be made in the laboratory which can lead to many useful and valid conclusions. One of the simplest, but most useful, measurements is that of thermal coupling, which is fully described in the next section.

### 3. Thermal Coupling

#### a. Skin Depth

For a good conductor, incident laser optical energy will be converted to thermal energy in a distance known as the skin depth  $\delta$ , with

$$\delta = \left( \frac{1}{\pi \sigma \mu \nu} \right)^{1/2} \quad (3)$$

The magnitude of  $\delta$ , compared to the thickness of the target, will determine whether the energy conversion process is a surface phenomenon. For the target material used in this thesis, the relative permeability will be close to unity [Ref. 16: p. 214]. Then  $\mu = \mu_0 = 1.2566 \times 10^{-6}$  H/m. Using the values of conductivity from Appendix A, the skin depths of the four target materials utilized in this thesis are tabulated in Table 2. It should be pointed out that silicon at room temperature is not a good conductor. Its approximate skin depth at room temperature may be taken to be  $10^{-3}$  cm at 1.06 micron incident radiation [Ref. 17: p. 9].

#### b. Heat Conduction and Thermal Diffusivity

Once optical energy is converted to thermal energy, the heat conduction problem must be solved. Metheny [Ref. 6] and Ready [Ref. 15] discuss in some detail the validity and solution of the heat conduction problem.

Heat flow through a target is dependent on several characteristics of the material. These include the thermal

conductivity  $K$ , specific heat  $c$ , and density  $\rho$ . The important factor which appears in the heat conduction equation is

$$\kappa = \frac{K}{\rho c} \quad (4)$$

and is referred to as the thermal diffusivity ( $\text{cm}^2/\text{sec}$ ). The heat conduction equation contains the diffusivity and may be written [Ref. 15: p. 70] as

$$\nabla^2 T(\bar{r}, t) - \left(\frac{\rho c}{K}\right) \frac{\partial T(\bar{r}, t)}{\partial t} = -\frac{Q(\bar{r}, t)}{K} \quad (5)$$

Thermal diffusivity determines how rapidly a material will accept and conduct thermal energy. Appendix A lists values of thermal diffusivity for several metals. A low value corresponds to poor thermal diffusion and means that heat does not penetrate well into the material. A high value suggests that heat may diffuse rapidly from the surface preventing damage mechanisms on the surface from becoming established.

The diffusion time  $\tau_d$  in seconds for heat flow through a target of thickness  $d$  may be expressed as

$$\tau_r = \frac{d^2}{4 \kappa} \quad (6)$$

where  $\kappa$  is the thermal diffusivity [Ref. 18]. This is for axial heat flow, as opposed to radial heat flow across the target which may be similarly expressed as

$$\tau_r = \frac{r_0^2}{4\kappa} \quad (7)$$

where  $r_0$  is the laser focal spot radius. If the axial diffusion time  $\tau_d$  is much less than the radial diffusion time  $\tau_r$ , then thermal measurements taken at the back surface of a target will be proportional to the absorbed energy [Ref. 18]. Stated another way,  $\tau_d \ll \tau_r$  is equivalent to  $d \ll r_0$ . The target thickness must be sufficiently small in comparison to laser spot size to assume a one-dimensional heat conduction problem [Refs. 9, 10]. Diffusivity times for the target materials used in this thesis are tabulated in Table 3.

Equation 6 can be used in another extremely useful manner, that is, to compute the axial diffusion time for a particular depth into the target. For example, by letting  $d$  equal the skin depth of TiC from Table 2, the diffusion time is  $3 \times 10^{-11}$  seconds. This demonstrates that for a 20 nanosecond laser pulse, the incident laser energy penetrates the skin depth of the target very early in the laser pulse. This corresponds to the material reaching its vaporization point early in the laser pulse which is shown to be the case by the data of Table 1.

In comparing the data in Table 3, the axial diffusion time is smaller than the radial diffusion time in both materials, but not enough to use a strictly one-dimensional heat conduction problem. It is also seen that aluminum is a much better conductor of heat than stainless steel. But in both cases, the axial diffusion time is long compared to the laser pulse duration (20 nsec FWHM) so that radial diffusion becomes a factor when thermal data is taken at the back surface of the target.

c. Thermal Coupling Coefficient

The effectiveness with which incident laser energy is coupled thermally to a target can be specified by the thermal coupling coefficient  $\alpha$ . This coefficient is essentially a ratio of absorbed energy per pulse to incident laser energy. For a one-dimensional heat conduction problem, Hettche et al [Ref. 9] and Metz et al [Ref. 10] both define the thermal coupling coefficient as

$$\alpha = \frac{d \rho c \Delta T}{E_D} \quad (8)$$

Figure 6 shows a typical distribution of thermal coupling for two different pressures. At both pressures, the coupling coefficient rises rapidly above some threshold value of energy density. This abrupt increase in the thermal coupling coefficient corresponds to the enhanced coupling

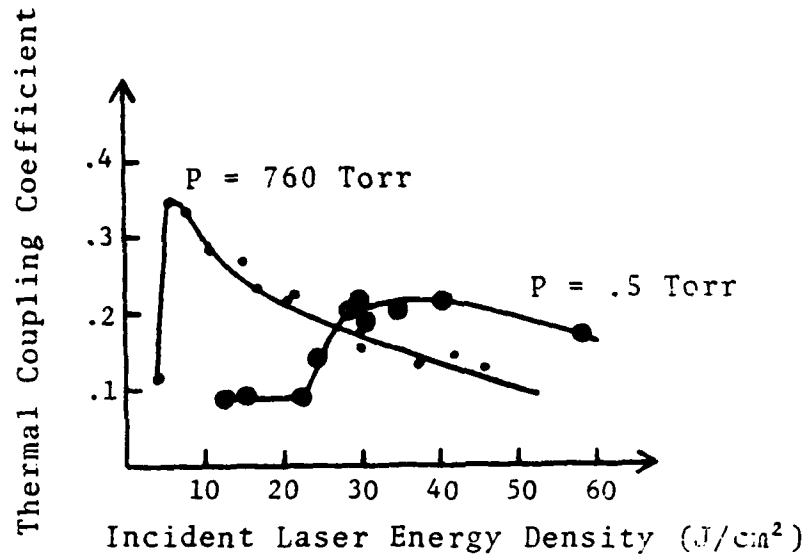


Figure 6. Pressure Dependence of Thermal Coupling for Aluminum [Ref. 12].

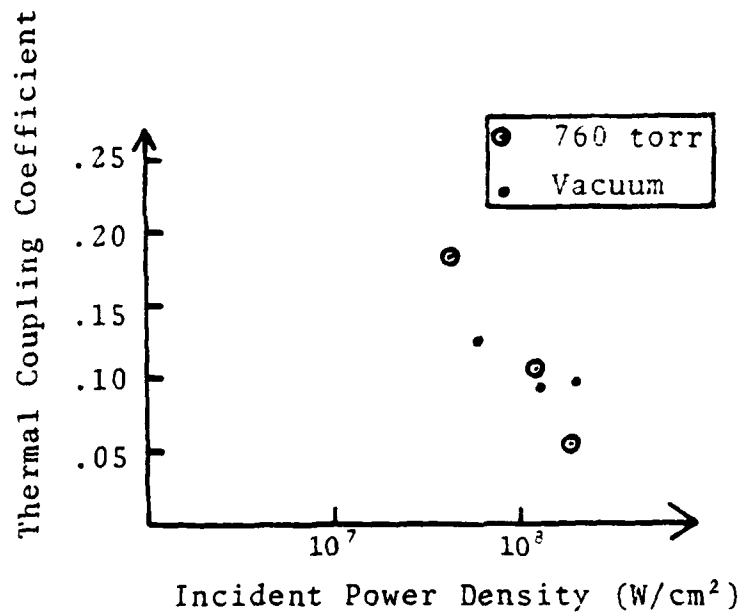


Figure 7. Thermal Coupling Coefficient of Aluminum for 1.06 Microns as a Function of Incident Power Density. A 5 microsecond laser pulse was used [Ref. 9].

by the plasma as discussed in the earlier section on energy absorption. Enhanced coupling occurs with the onset of a surface breakdown plasma which is highly absorbing. For increasing values of energy, the coupling actually decreases due to the formation of an LSA wave.

As Figure 6 illustrates, thermal coupling is highly dependent on pressure. At reduced pressures, the abruptness of the enhanced coupling becomes less pronounced and occurs at larger values of energy. However, once the enhanced coupling occurs, it is greater than the coupling at atmospheric pressure due to the reduced opacity and velocity of the LSA wave [Ref. 12].

For a target in vacuum, the thermal coupling data of Figure 7 illustrate the decrease in coupling with increasing power density. It is important to note that for these results there is little variation between targets shot in air and vacuum.

In general, thermal coupling is dependent on incident energy density, target material, pressure, wavelength, and laser spot size. As previously mentioned, a reliable determination of thermal coupling can yield valuable information concerning the coupling of energy to a target by a laser beam. With an understanding of the energy coupling mechanism, a model for explaining laser-surface damage mechanisms can be formulated. A reliable measurement

of thermal coupling depends on target thickness being sufficiently small compared to laser spot size so that Equation 8 can be used.

### C. PLASMA-SURFACE INTERACTIONS

#### 1. Sheath Effects

Damage due to plasma-surface interactions has been an area of concern for two decades in magnetic confinement fusion programs. When a plasma is confined, it establishes a potential distribution such that the plasma potential is positive in relation to the walls. This is because electrons, having a higher thermal velocity than the ions in the plasma, are lost to the walls faster. The wall potential, consequently, is negative with respect to the plasma. In CGS units, this potential  $V_f$  is determined to be [Ref. 19]

$$V_f = -\frac{kT_e}{2e} \ln \left( \frac{M_i}{2\pi m} \right) \quad (9)$$

Debye shielding assures the maintenance of the plasma quasi-neutrality by confining the wall potential variations to a thin layer, called a sheath, of several Debye lengths in thickness. The Debye length [Ref. 19], also defined in CGS units, is

$$\lambda_D = \frac{kT_e}{4\pi ne^2} \quad (10)$$

The sheath thus acts as a barrier, constantly adjusting its potential so that the flux of electrons that have enough energy to get over the potential barrier to the wall is just equal to the flux of ions reaching the wall. Thus the terms floating potential and sheath potential are usually applied to this constantly changing potential.

## 2. Unipolar Arcing

Several processes lead to damage of the wall material when it is exposed to the plasma particle and photon fluxes. These damage processes include physical and chemical sputtering, blistering, evaporation, and unipolar arcing [Ref. 19]. Unipolar arcing has been shown to be the dominant mechanism for introducing impurities in the DITE tokamak [Ref. 20]. Much intensive research in recent years has focused on the study of this damage mechanism. Laser-produced plasmas on a variety of targets have been used to simulate the conditions inside a vacuum containment vessel so that the unipolar arc process may be more closely examined.

Unipolar arcing was first described by Robson and Thoneman [Ref. 21], and later expanded by Schwirzke and Taylor [Ref. 14]. Arcing occurs if the sheath potential, defined by Equation 9, is high enough to ignite and sustain an arc. Minimum arc current and voltage are on the order of 10 amps and 10 volts, respectively [Ref. 14]. With a sufficiently high sheath potential, comparable to the

ionization energy of the constituent atoms of the wall material, electrons are emitted from surface spots to the plasma (Figure 8). These surface spots, called cathode spots, may be due to surface imperfections or lattice structure inhomogeneities. The electrons flowing from these cathode spots reduce the plasma potential and more electrons are able to reach the wall thus closing the current loop. The wall acts as both the cathode and anode, thus the term unipolar arcing. One other driving mechanism, in addition to the sheath potential, is necessary to initiate and sustain an arc. The ion density must increase above the localized cathode spots in order to facilitate electron flow from the surface. Ion flux may increase above the surface imperfections and lattice inhomogeneities mentioned above due to the increased electric field at these aberrations. An increase in ion flux thus will aid in the establishment of an electric field,  $E = V_f/\lambda_D$ , which continues to drive the arcing process. The increased ion density above a cathode spot increases the plasma pressure, and thus the electric field,  $E_{arc}$ . This increased pressure gradient also leads to a radial electric field  $E_r$  as explained by Schwirzke and Taylor [Ref. 14]. The effect of the radial field is to reduce the potential around the cathode spot thus permitting more electrons to flow to the surface and close the current loop.

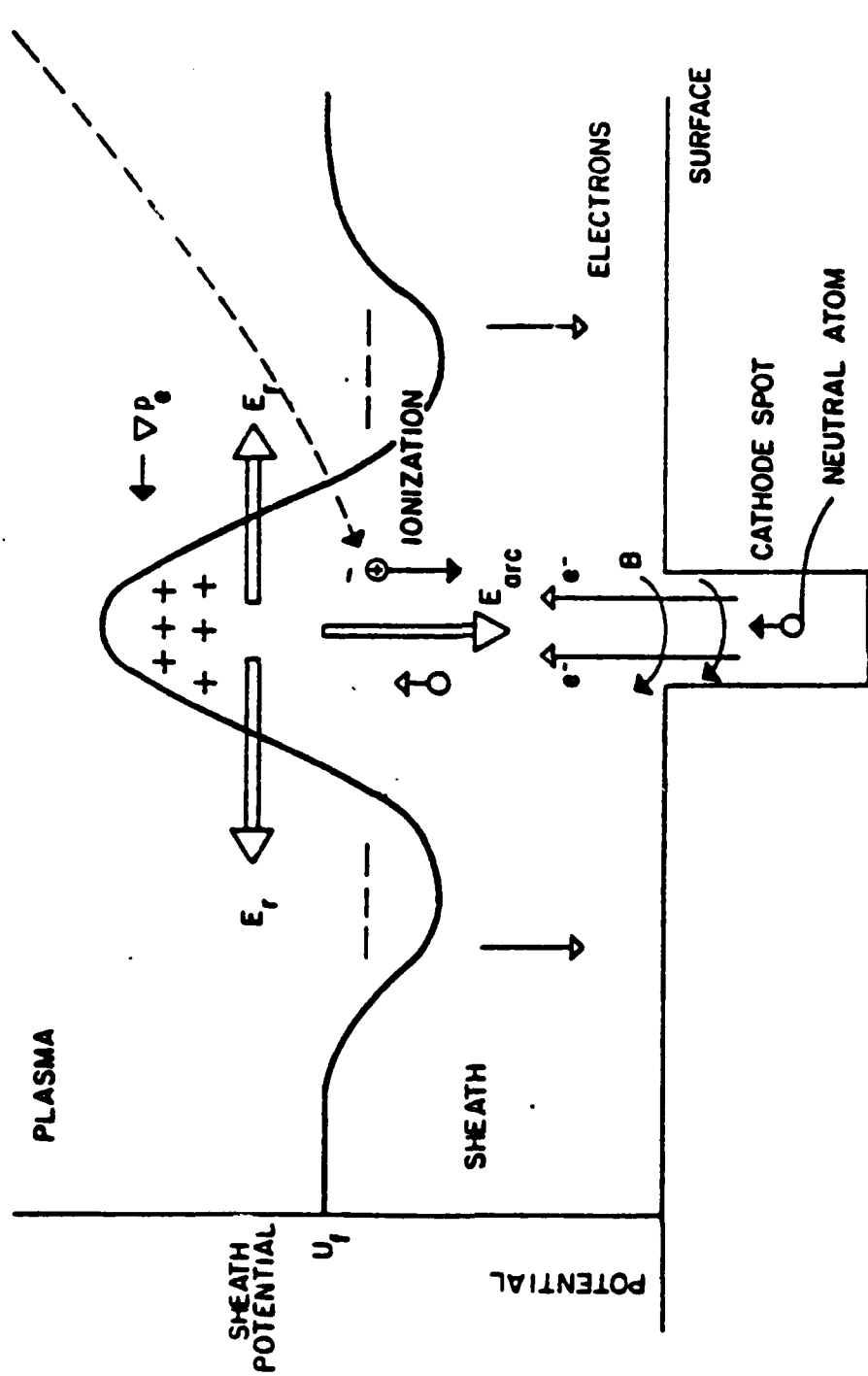


Figure 8. Unipolar Arc Model

Unipolar arcing is a microstructure phenomenon. For stainless steel, cathode craters have a diameter of 1 micron and a depth of 3-6 microns [Ref. 14]. As laser pulse duration increases, the crater rim expands to a larger diameter. Typical crater density has been found to be  $300,000 \text{ cm}^{-2}$  [Ref. 14]. The high density of these arc craters leads one to conclude that unipolar arcing is a serious damage mechanism that leads to erosion of a surface.

The effect of unipolar arcing for various types of materials has been studied to determine whether material characteristics have any effect in reducing the arcing damage. Schwirzke et al [Ref. 19] and Metheny [Ref. 6] found that stainless steel targets were heavily damaged by unipolar arcing, but TiC-coated stainless steel exhibited no apparent large unipolar arc crater damage. It was postulated by Schwirzke that the higher melting temperature and resistivity of TiC may inhibit arcing. Metheny also showed a direct relationship between arcing damage and thermal coupling, proposing unipolar arcing as a possible mechanism for increased thermal coupling.

### 3. Discussion

It is apparent that laser-target interaction with its attendant plasma-induced arcing is a dynamic process which must be described in terms of constantly changing variables. Such variables include, but are not limited to, plasma temperature and density, laser power and pulse

duration, surface area exposed, target material and surface preparation, and physical properties of the target. It appears that unipolar arcing can be reduced by lowering the plasma electron temperature or density [Ref. 20]. However, a larger laser power density will lead to heating of the target and plasma, thus increasing damage due to arcing. The surface area exposed to the plasma must be large enough to collect the required current to support arcing. Thus, unipolar arcing in tokamaks may be reduced by subdividing exposed areas with insulating strips [Ref. 22]. Each of these subdivided areas would have to be less than the minimum area required to support arcing. This technique is not practical when dealing with a laser-produced plasma, where the small target surface is covered by a high number of arc craters. Target material and surface preparation will play a large role in determining arcing damage effects and thermal coupling. As mentioned above, a TiC coating was thought to inhibit unipolar arcing as compared to metal surfaces. This thesis investigated the effect of coating a target with pure silicon and TiC. Results are discussed in Sections IV and V. Finally, material physical properties, as tabulated in Appendix A, will have a direct influence on thermal coupling and unipolar arcing. Some of these connections are discussed in Section V.

### III. EXPERIMENTAL DESIGN

#### A. EQUIPMENT

The equipment utilized in this thesis to create and evaluate plasma-surface interactions included a neodymium-glass laser, an evacuated test chamber, a laser energy meter, thermocouples with associated recording equipment, and a polaroid camera. Target surface effects were studied with a scanning electron microscope, and material specular reflectivity was evaluated with a Nd:YAG CW laser. Figure 9 is a schematic of the Nd:glass laser and test arrangement.

##### 1. Laser System

A KORAD K-1500 Q-switched neodymium-doped glass laser [Ref. 23] was used to irradiate the targets. Incident laser energy was varied by inserting neutral density filters of varying transmittance in the beam path. For low energy shots the laser amplifier was not fired. Laser energies on target between .0075 and 10 joules were obtained by these techniques. Nominal beam pulse half width of the laser was 20 nanoseconds. This small pulse width is achieved by using a pockels cell between the oscillator and the rear reflector. The beam was focused to various spot sizes on the target to provide further variation in power density at the target. Laser energy at each shot was measured using a Laser Precision RK-3200 Pyroelectric Energy Meter, with a RE 549 detector reading via an 8% splitter in the main beam.

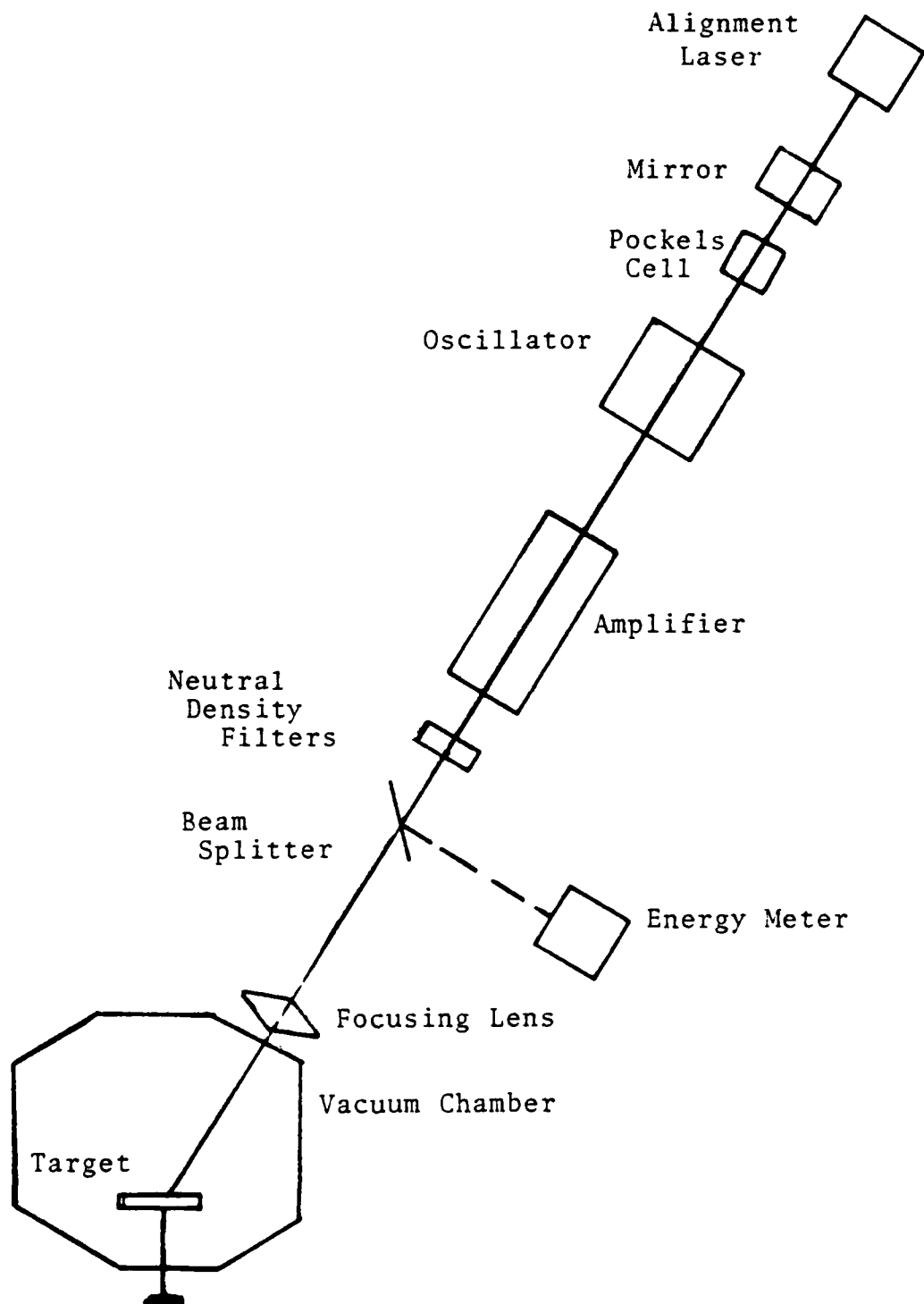


Figure 9. Schematic of Pulsed Laser and Test Chamber Arrangement.

## 2. Target Test Chamber

The target test chamber is a cube of unbaked aluminum with an internal volume of 12.9 +/- 0.3 liters, mounted on a vacuum system capable of providing up to  $10^{-6}$  Torr. The vacuum system uses a displacement forepump and a diffusion pump with a liquid nitrogen-cooled baffle to achieve vacuum.

The laser beam was aligned 32 degrees from normal to the target surface. Four targets were mounted on a target holder, and a probe was used to hold the mounting in the chamber and to rotate the targets between shots without the need to break vacuum. Figure 10 is a diagram of the target test chamber.

## 3. Thermal Data Recording

Thermal data was recorded using beaded thermocouples fabricated from 28 gauge copper-constantine pairs connected to a Fluke 2190A Digital Thermometer, which was capable of measuring temperature to a tenth of a degree. The temperature variation was recorded with a Honeywell Electronic 19 strip chart recorder. A special mounting plate using rubber insulation behind the test targets was used to minimize the thermal transport out of the target, and to insure close contact between the thermocouple and target. System accuracy in the measurement of temperature change was +/- 0.05 Kelvin. Upon completion of the data measurements, the strip charts were time averaged for the five second periods before and

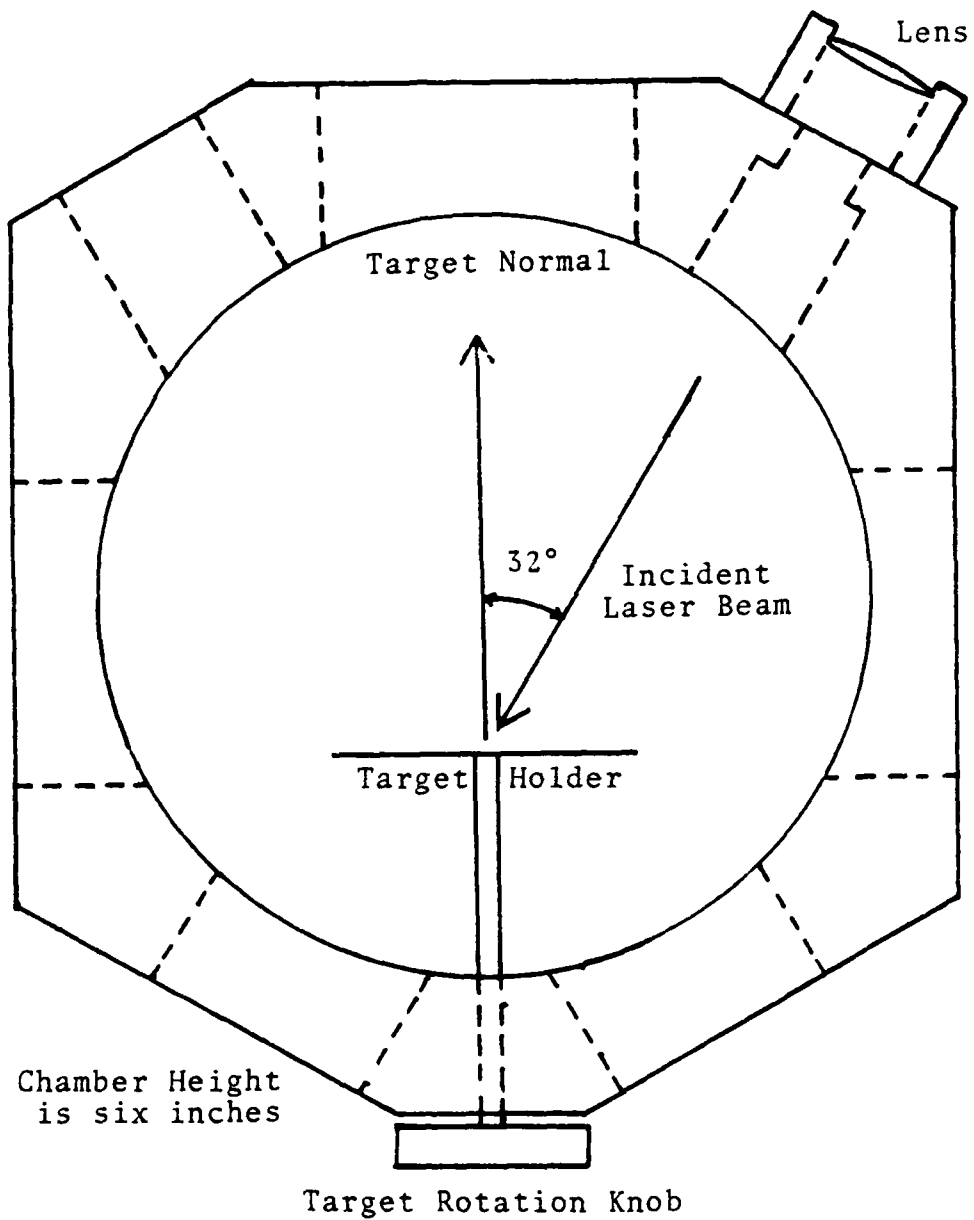


Figure 10. Aluminum Vacuum Chamber Diagram, Top View.

after each shot to obtain a temperature rise to a thousandth of a degree.

#### 4. Scanning Electron Microscope

The Cambridge Stereoscan S4-10 scanning electron microscope was used extensively during this thesis for examination and photography of test targets both before and after irradiation. The Stereoscan has a direct reading magnification system with a useful range between 20X and 100,000X with corresponding scanned areas of 5 mm and 2 microns square on the specimen. The greater magnification available was critical to detailed examination of the test surfaces.

#### 5. CW Laser System

A General Photonics Corporation YAG-TWO, CW neodymium-doped yttrium aluminum garnet laser rated at 2 watts was used to measure specular reflectivity of tested materials. This laser is water cooled, has a line width of about 10 GHz, and produces an unpolarized beam of about 2 mm diameter. Two power meters, a Scientech 362 Power and Energy Meter with a Scientech model 360001 detector, and a Coherent Model 201 Power Meter and detector, were used to measure beam power incident on the target and that reflected specularly at 30 degrees to normal.

### B. PROCEDURE

#### 1. Plasma Onset

Plasma onset was determined using the vacuum chamber at  $10^{-6}$  Torr, firing only the laser oscillator, and varying

the beam intensity with neutral density filters. Determination of actual plasma formation was made with photographs taken with a hand held polaroid camera. The photographs were taken with the lab darkened and the camera shutter held open manually throughout the laser shot. A 1.06 micron filter was used to prevent beam radiation from affecting the photograph. When plasma initiation energy was determined for a particular material, beam spot size was measured by placing exposed polaroid film on the target holder and firing at several spots with the same beam energy. The area of the spots was measured and averaged, and the average size was used for energy and power density calculations.

## 2. Thermal Coupling

Thermal coupling was investigated using a special target holder and the vacuum chamber at  $10^{-6}$  torr. Laser energy on target was held at a selected value high enough to achieve discernible temperature changes, yet as low as practicable to remain as close as possible to plasma onset energy. Laser spot size was measured directly from irradiated targets, and target thickness and mass were recorded.

## 3. Surface Damage

Details of surface damage were investigated with the scanning electron microscope after both the plasma onset and the thermal coupling tests. Samples were ultrasonically cleaned in an acetone bath and stored in a desiccant chamber

prior to examination. Where indicated, selected samples were metallurgically etched to test for specific surface materials.

#### 4. Target Specular Reflectivity

The specular reflectivity of test materials was measured using a low power CW Nd-YAG laser, the General Photonics Corporation YAG-TWO. The samples were placed in the laser beam with an angle of incidence of 30 degrees to normal. The beam power was determined using a splitter and a Scientech 362 power meter prior to reflection from the target. Beam power reflected specularly from the target was measured with a Coherent Model 201 power meter. The equipment arrangement is schematically shown in Figure 11.

#### 5. Sample Preparation

Three categories of surface preparation were used during the course of this thesis; unpolished machined or rolled surfaces, mechanically polished surfaces, and mechanically polished and coated surfaces.

2024 aluminum was used in the unpolished, polished, and polished and coated forms. The unpolished surface was a rolled surface, as received from the vendor. The mechanically polished samples were prepared using standard metallurgical techniques with final polishing done with a 0.05 micron Magomet paste. Several aluminum samples polished in this fashion were coated by the Naval Research Laboratory (NRL)

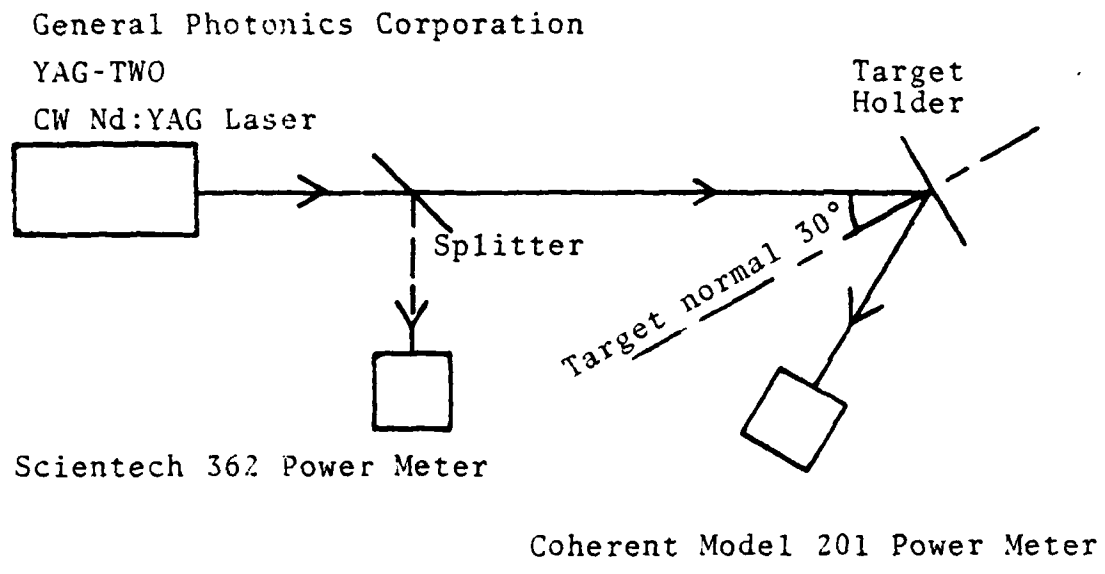


Figure 11. Schematic of Equipment Arrangement for Specular Reflectivity Measurement.

with silicon. Coatings of approximately 0.2 and 1.0 micron were applied by sputtering.

The 1 micron coatings were applied in a vacuum system in an atmosphere of purified argon at 0.109 torr. The aluminum was not preheated, but did reach a temperature of about 300 degrees Celsius during the process. The silicon was sputtered from a high purity target at 500 watts for 60 minutes. The 0.2 micron coatings were applied under the same conditions by sputtering for 12 minutes.

SS-304 was also used in the unpolished, polished, and polished and coated forms. The unpolished surfaces were machined, and tended to be very irregular. The polished materials were prepared in the same manner as the aluminum, but with a final slurry of 0.05 micron Gamma Alumina. Several polished SS-304 samples were also coated by NRL with silicon. The silicon coatings were applied in a purified argon atmosphere at 0.073 torr. The SS-304 was preheated with 6 amperes of current to approximately 775 degrees Celsius, then the silicon coat was sputtered from a purified silicon target at 750 watts for 70 minutes. The resulting coatings were 1 to 2 microns thick.

A TiC coating over SS-304 foil was also used during this investigation. The TiC films were applied to a 0.5 mm thick SS-304 foil at the University of California at Los Angeles by the ARE deposition technique. A detailed description

of this process is contained in Keville and Lautrup [Ref. 1].  
The substrate temperature used to prepare the material used  
here was 550 degrees Celsius.

#### IV. EXPERIMENTAL RESULTS

##### A. PLASMA ONSET

Plasma onset was investigated for SS-304 foil coated with TiC, and for 2024 aluminum with a polished surface, an unpolished surface, and a polished surface coated with silicon. All tests were conducted in the vacuum chamber at  $10^{-6}$  torr on targets which had been prepared, cleaned with acetone, and placed in a desiccator overnight prior to testing.

##### 1. TiC-Coated SS-304 Foil

The TiC samples were irradiated using two different variations of the basic equipment arrangement. Targets number 5 through 20 were shot with the splitter for the power meter located in front of the filter combination. The results from this arrangement were very inconsistent, and prompted a change to an arrangement placing the splitter after the filter combination. Results are listed in Table 4. The value selected as plasma onset was  $5.8 \text{ MW/cm}^2$ .

##### 2. Unpolished 2024 Aluminum

Unpolished aluminum targets were irradiated using the basic equipment arrangement shown in Figure 9. The results are listed in Table 5. Table 5 indicates that photographic evidence of plasma formation was found for all values of power density above  $5 \text{ MW/cm}^2$ , while between 4 and  $5 \text{ MW/cm}^2$  the evidence points to the formation of either a

well-formed plasma, a dim plasma, or no plasma at all. Allowing for variations in equipment and target surface conditions, an approximate value of 4 MW/cm<sup>2</sup> was taken as the plasma onset power density.

3. Polished 2024 Aluminum

Polished aluminum targets were shot using the same equipment arrangement as above. The results are listed in Table 6. As indicated in the table, one target was irradiated several times to establish the proper range for onset, then successive targets were irradiated to confirm the approximate value. 18 MW/cm<sup>2</sup> was selected as the approximate value of power density at plasma onset.

4. Polished 2024 Aluminum Coated with 0.2 Micron Silicon

Targets coated with 0.2 micron silicon were irradiated using the same equipment arrangement as before. A single target was used and irradiated at several different positions. The results are listed in Table 7. Due to the limited number of samples of this material available, the results are based on a much smaller number of shots, and are not definitive. The very approximate value assigned to power density for plasma onset was 6 to 7 MW/cm<sup>2</sup>.

5. Polished 2024 Aluminum Coated with 1 Micron Silicon

Targets coated with 1 micron of silicon were tested in the same manner as above, again with a single sample being used. The results are listed in Table 8. The approximate power density for onset was chosen as 9 to 10 MW/cm<sup>2</sup>.

## B. THERMAL COUPLING

This study considered thermal coupling to 2024 aluminum, SS-304, and these same materials coated with silicon. Equipment sensitivity limitations prevented coupling measurements at plasma onset power densities. A nominal power density of  $10^8$  W/cm<sup>2</sup> was selected to optimize equipment capabilities. Although sample thickness made the validity of this assumption somewhat marginal, heat conduction was considered to be a one-dimensional function of target thickness. The results are considered to be valid for targets of the same base material, as samples within each material group were all of similar geometric shape and size. Comparisons between different material groups can not be made based on this data. The coupling coefficient was computed for each target using the one-dimensional assumption and Equation 8. Results are presented grouped by base metal.

### 1. 2024 Aluminum

Four different surface preparations of 2024 aluminum were exposed to the plasma-surface interaction and tested for thermal coupling: a commercially supplied unpolished surface, a mechanically-polished surface, and mechanically-polished surfaces coated with either 0.2 or 1 micron silicon.

#### a. Unpolished Aluminum

The unpolished aluminum targets were irradiated with the laser in the Q-switched mode, with the beam energy

attenuated by a neutral density 40% transmission filter. The laser beam was offset from target center in some cases to allow two shots on each target. The resulting beam was focused onto the target with a 40 cm converging lens to achieve an apparent spot diameter of approximately 0.55 cm. Spot diameter was measured using exposed polaroid film. Resulting energies at the target ranged from 1.79 to 2.59 joules, with associated power densities of 320 to 462 MW/cm<sup>2</sup>. Results are listed in Table 9. Average value of the coupling coefficient was 0.0138.

b. Polished Aluminum

The polished aluminum samples were tested using the same procedure as above. Energy at the target ranged from 1.88 to 3.01 joules, with corresponding power densities of 335 to 483 MW/cm<sup>2</sup>. The results are listed in Table 10. Average value of the coupling coefficient was 0.00838.

c. Polished Aluminum Coated with 0.2 Micron Silicon

The targets coated with 0.2 micron silicon were tested using the same procedure as above. Energy on the target ranged from 1.90 to 2.49 joules, with associated power densities of 339 to 429 MW/cm<sup>2</sup>. Test results are listed in Table 11. Average value for the coupling coefficient was 0.0175.

d. Polished Aluminum Coated with 1 Micron Silicon

The 1 micron targets were tested using the same procedure as above. Energy on the target ranged from 1.77

to 3.09 joules, with corresponding power densities of 316 to 495 MW/cm<sup>2</sup>. Complete test results are listed in Table 12. The average value of the coupling coefficient was 0.00718.

The small number of targets available for both the 0.2 and 1 micron coatings render the results very tentative. Further testing and corroboration would be required before any firm conclusions could be drawn from the obtained results.

## 2. SS-304

Three different surface preparations of SS-304 were exposed to the plasma-surface interactions and tested for thermal coupling: a machined surface; a mechanically-polished surface; and a mechanically-polished surface coated with 1 to 2 microns.

### a. Unpolished SS-304

The unpolished SS-304 targets were tested using the same arrangement as that for the aluminum targets. Energies at the target ranged from 2.03 to 2.82 joules, with corresponding power densities from 363 to 453 MW/cm<sup>2</sup>. Complete results are listed in Table 13. The average value of the coupling coefficient was 0.0188.

### b. Polished SS-304

The polished SS-304 targets were tested using the same procedure as above, except that no single target was shot more than one time due to target size. The energy at the target varied from 1.78 to 2.85 joules, with corresponding

power densities from 318 to 458 MW/cm<sup>2</sup>. Complete results are listed in Table 14. The average value of the coupling coefficient was 0.0193.

c. Polished SS-304 Coated with Silicon

The silicon-coated targets were tested using the same procedure as with the polished stainless steel. The energy at the target varied from 2.06 to 2.42 joules, with corresponding power densities from 368 to 433 MW/cm<sup>2</sup>. The average value of the coupling coefficient was 0.0150. Complete test results are listed in Table 15.

C. SURFACE DAMAGE AND UNIPOLAR ARCING

Surface damage effects were examined for all materials tested in two general power ranges, at plasma onset and in the vicinity of 10<sup>8</sup> MW/cm<sup>2</sup>. The study was conducted with the Cambridge Stereoscan S5-10 scanning electron microscope.

1. Aluminum Targets at Plasma Onset

a. Unpolished 2024 Aluminum

The surface finish typical of the unpolished aluminum targets is seen in Figure 12. The surface as shown was cleaned with acetone, but no attempt was made to remove any of the tightly adhering surface material. After exposure to laser radiation of sufficient intensity to reach plasma onset, the surface was examined by SEM again. Small areas of surface melting and cratering were seen near sites where foreign material was adhering to the surface. Figure 13 is



Figure 12. Unpolished 2024 Aluminum before Irradiation, SEM 1200X.



Figure 13. Unpolished 2024 Aluminum after Irradiation with 4 MW/cm<sup>2</sup> Plasma Onset Power Density, SEM 1100X.

an enlargement of a typical melted and cratered area. Typical crater size was estimated to be on the order of from one to a few microns in diameter, with depths of 2 to 4 microns.

b. Polished 2024 Aluminum

The as-polished aluminum surface is pictured in Figure 14. By comparison with the unpolished sample at this magnification, the most significant difference is the absence of particles adhering to the surface of the polished material. Near plasma onset the same regions of melting and arcing are evident in the polished material as are present in the unpolished sample. Figure 15 is a picture of an area of the polished target exhibiting arcing damage.

2. Silicon-Coated Aluminum at Plasma Onset

a. 0.2 Micron Silicon Coat on Polished Aluminum

Figure 16 is a SEM photograph of the 0.2 micron silicon coating prior to irradiation. The silicon was applied over a polished surface of which Figure 14 is typical. The coating itself appears bumpy and irregular, with bumps approximately 1 micron in diameter. Surface damage at the approximate power density required for plasma onset is pictured in Figure 17. The damage picture shows the silicon melted away from small spots, 1 to 3 microns across, and solidified into tiny spheres along the edge of the melt spots. The approximate density of melt spots in the plasma onset area is  $5 \times 10^7 \text{ cm}^{-2}$ .

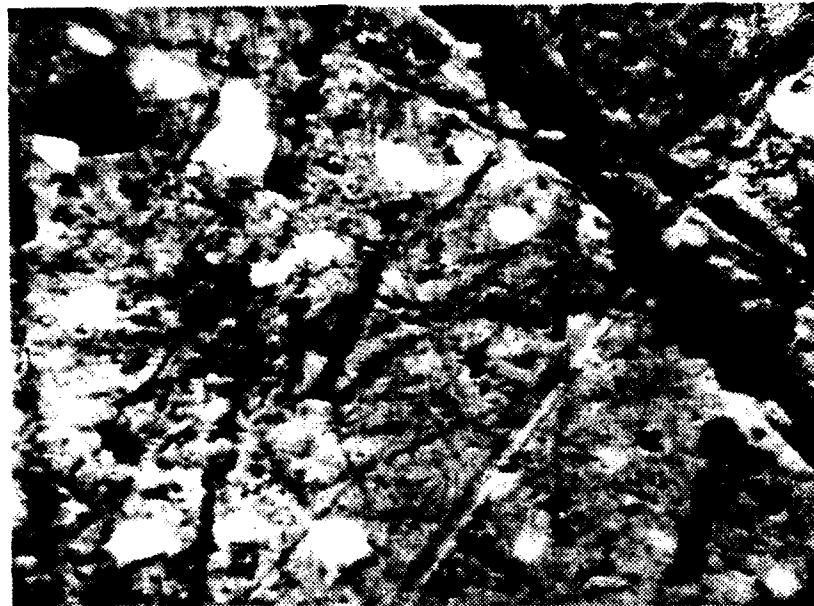


Figure 14. Polished 2024 Aluminum before Irradiation, SEM 5000X

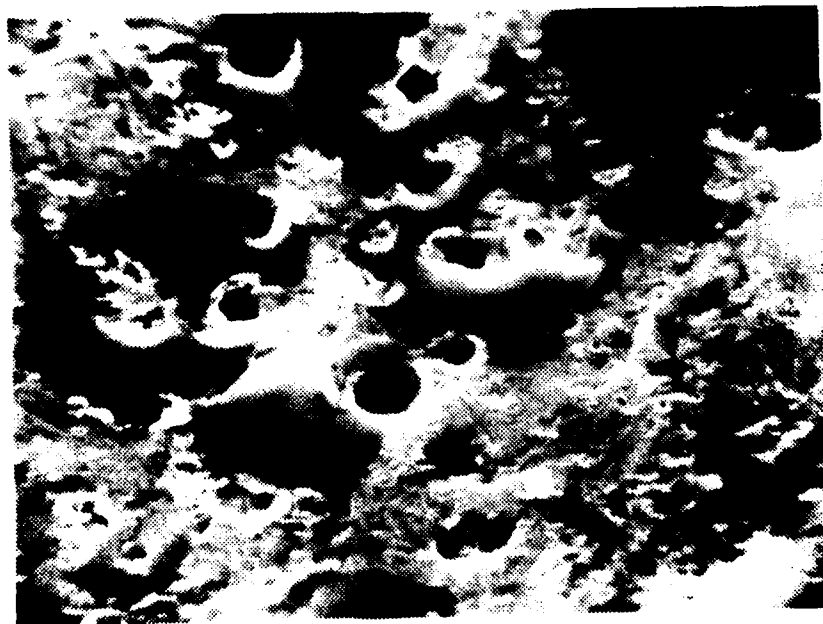


Figure 15. Polished 2024 Aluminum after Irradiation with 18 MW/cm<sup>2</sup> Plasma Onset Power Density, SEM 5000X

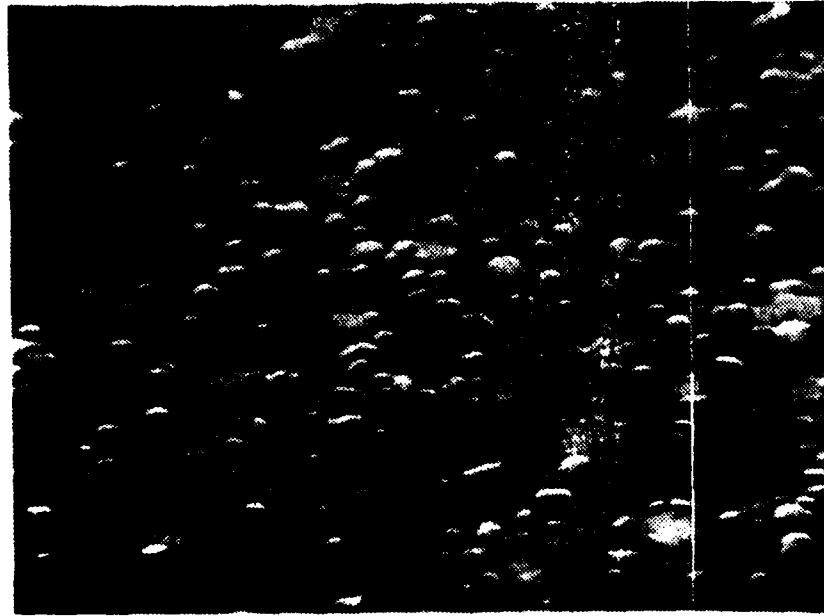


Figure 16. 0.2 Micron Silicon Coating over Polished 2024 Aluminum before Irradiation, SEM 5000X.

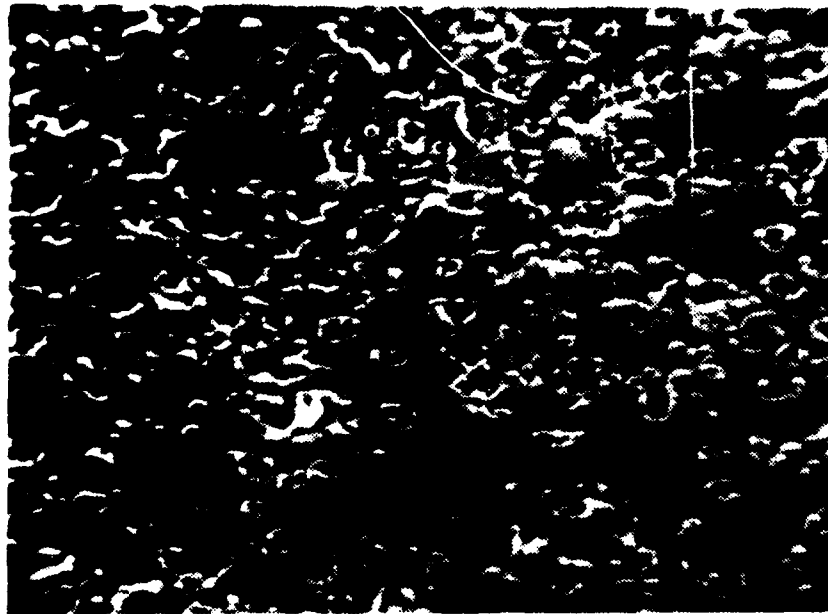


Figure 17. 0.2 Micron Silicon Coating over Polished 2024 Aluminum after Irradiation with  $7.4 \text{ MW/cm}^2$  Plasma Onset Power Density, SEM 5000X.

b. 1 Micron Silicon Coat on Polished Aluminum

Figure 18 is a SEM photograph of the 1 micron silicon coating prior to irradiation. This coat was also applied over a polished surface. The thicker coat is still bumpy, but does not appear as irregular as the thinner coat. After irradiation at the onset power density, tiny spheres of various degrees of irregularity appear, but the coating does not appear to have melted through. There are a few pieces of silicon flaked off the surface, each about 10 microns in diameter or less and about 0.5 micron thick or less. Figure 19 is a photograph of an area near the edge of the damaged region with several crater sites apparent. Figure 20 pictures a flaked area near the center of the damaged area.

3. TiC-Coated SS-304 at Plasma Onset

SS-304 targets coated with TiC had no discernible surface damage after exposure to laser radiation at plasma onset intensities. Figure 21 is a photograph of a typical TiC surface before irradiation, which is typical of the surface after irradiation at low power densities.

4. Aluminum Targets at  $10^8$  W/cm<sup>2</sup>

a. Unpolished 2024 Aluminum

At power densities in the vicinity of 400 MW/cm<sup>2</sup> the unpolished aluminum surface exhibited extensive melting and arcing. Typical arc crater size was 1 micron, with crater rims of 2 to 15 micron. Crater density was found to be about

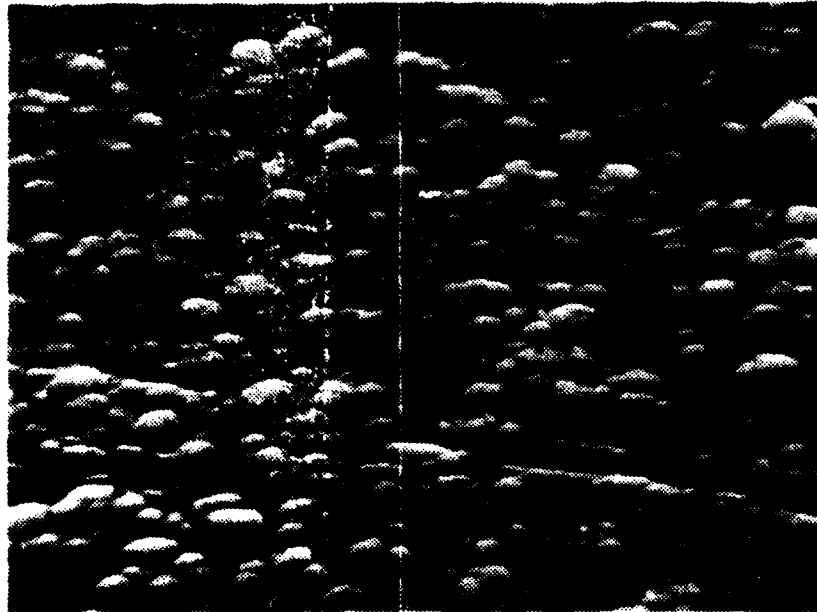


Figure 18. 1 Micron Silicon Coating over Polished 2024 Aluminum before Irradiation, SEM 5000X.

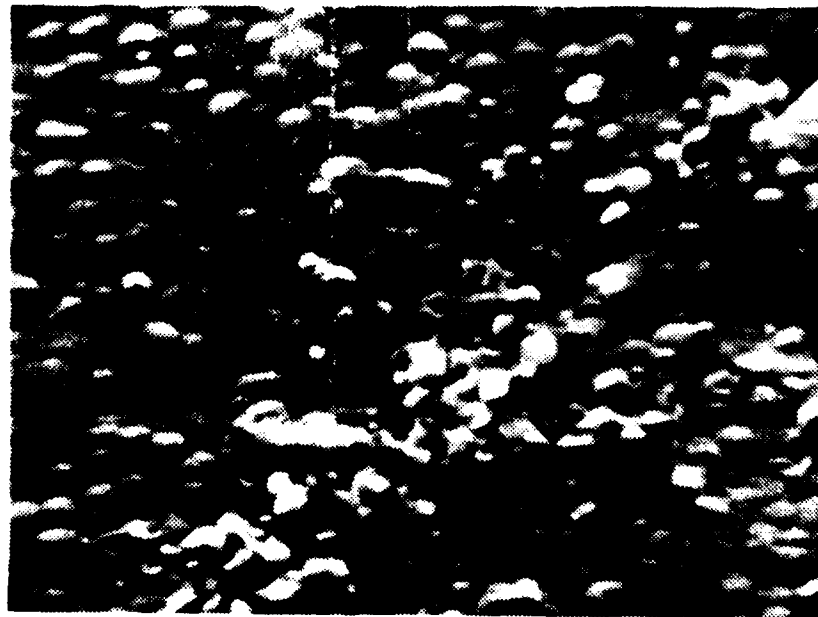


Figure 19. 1 Micron Silicon Coating over Polished 2024 Aluminum after Irradiation with  $9.8 \text{ MW/cm}^2$  Plasma Onset Power Density, Edge of Damage Area, SEM 5800X.

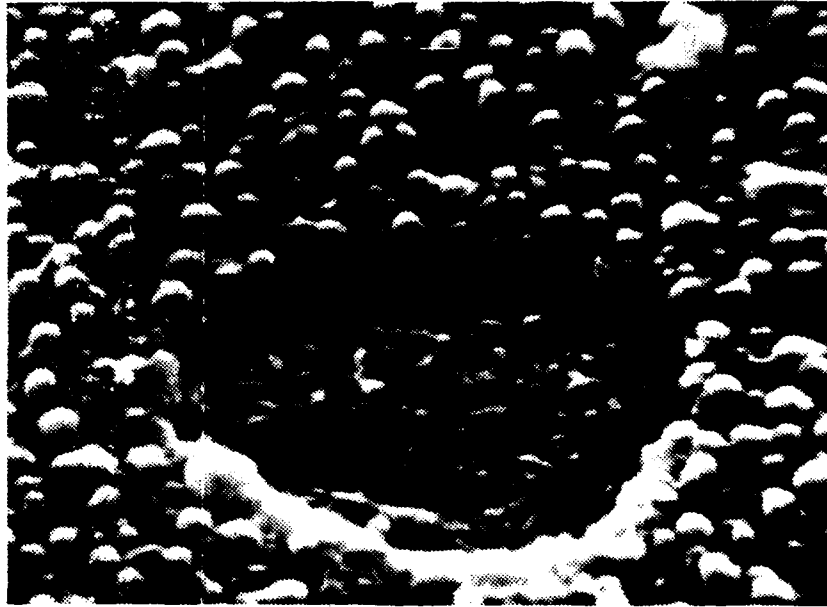


Figure 20. 1 Micron Silicon Coating over Polished 2024 Aluminum after Irradiation with  $9.8 \text{ MW/cm}^2$  Plasma Onset Power Density, a Flaked Area, SEM 5800X.

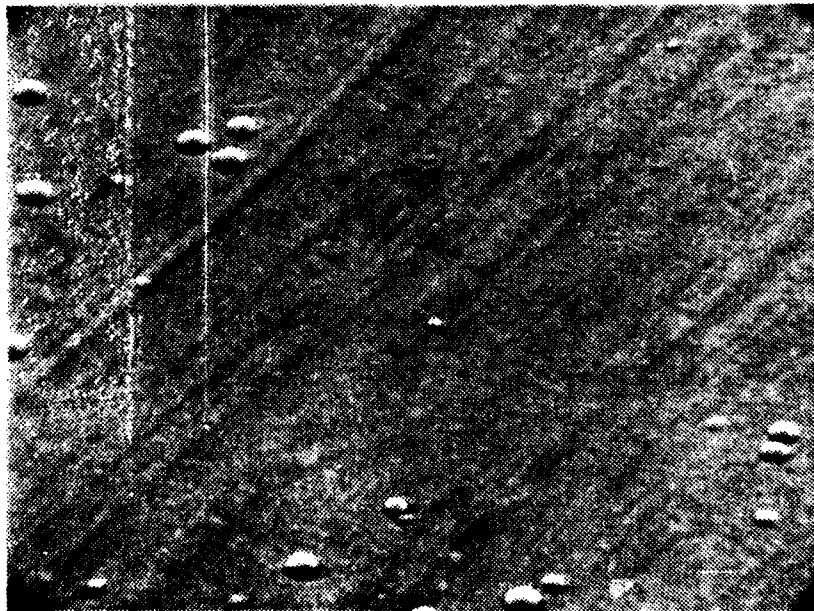


Figure 21. TiC Coating over SS-304 before Irradiation, SEM 490X.

$2 \times 10^5 \text{ cm}^{-2}$  or greater. At the edge of the irradiated area single arc craters formed and extended out of the melted region over otherwise undamaged material. The band of arcing was approximately 0.2 mm wide with a density of  $2 \times 10^5 \text{ cm}^{-2}$ . Figures 22 and 23 picture, respectively, the transition region from damaged to undamaged material, and a closeup of a large crater in the unipolar arcing band.

b. Polished 2024 Aluminum

The polished aluminum also exhibited extensive surface melting and cratering. The two phenomena occurred over approximately 60% of the irradiated surface compared with 95% for the unpolished aluminum and resulted in an arc density of approximately  $10^6 \text{ cm}^{-2}$  in the center of the damage area. Outside the melted regions arcing was also evident in the close vicinity. The arcing appeared in a band about 200 micron wide with a crater density of  $10^5 \text{ cm}^{-2}$ . Figures 24 and 25 picture typical melting and cratering in the center and cratering at the edge, respectively.

5. Silicon-Coated Aluminum at  $10^8 \text{ W/cm}^2$ .

a. 0.2 Micron Silicon Coat

At the high power density the localized melting evident at plasma onset power density has spread over essentially the entire irradiated area. Etching with a HF solution revealed no evidence of remaining silicon in the irradiated area. Within the melted area there was extensive

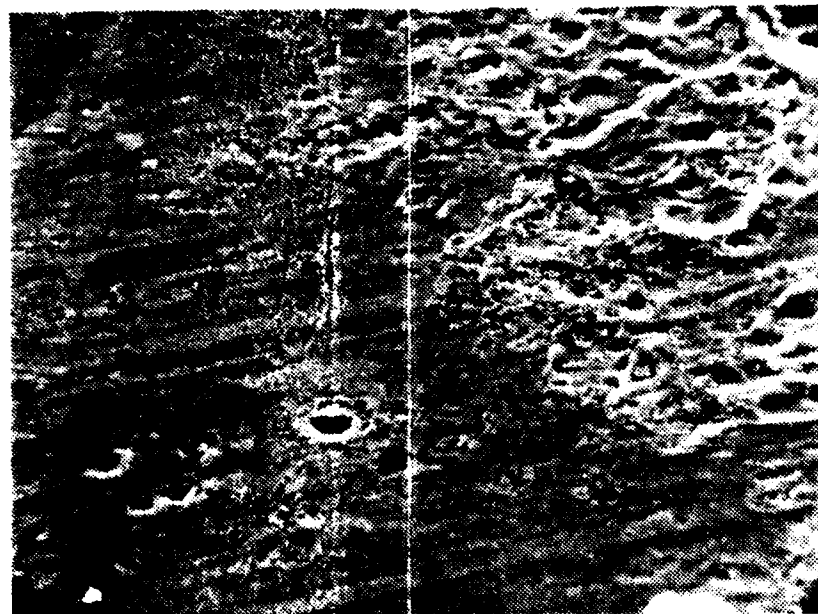


Figure 22. Unpolished 2024 Aluminum After Irradiation with 400 MW/cm<sup>2</sup>, Edge of Damage Spot, SEM 550X



Figure 23. Large Crater in Unmelted Region of Unpolished 2024 Aluminum Target, SEM 5500X.

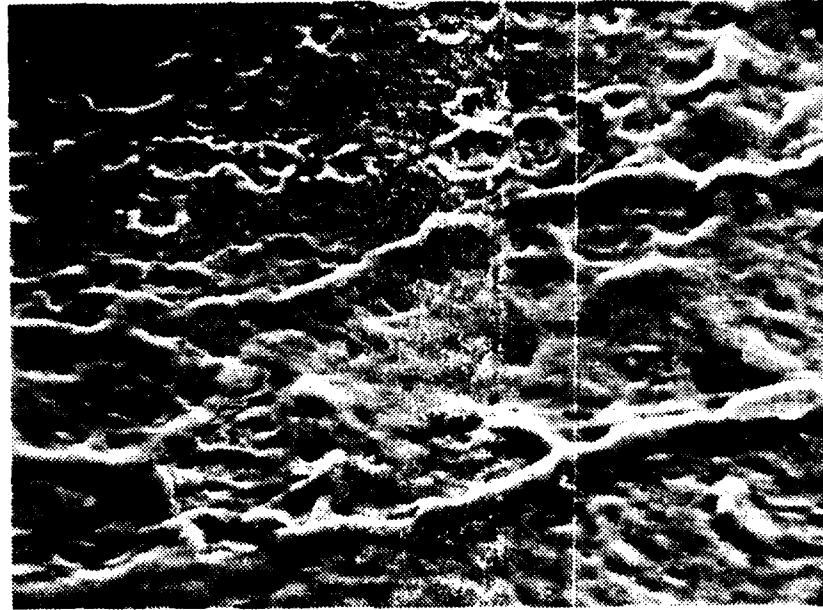


Figure 24. Polished 2024 Aluminum after Irradiation with  $400 \text{ MW/cm}^2$ , Typical Melted and Arced Area, SEM 475X.

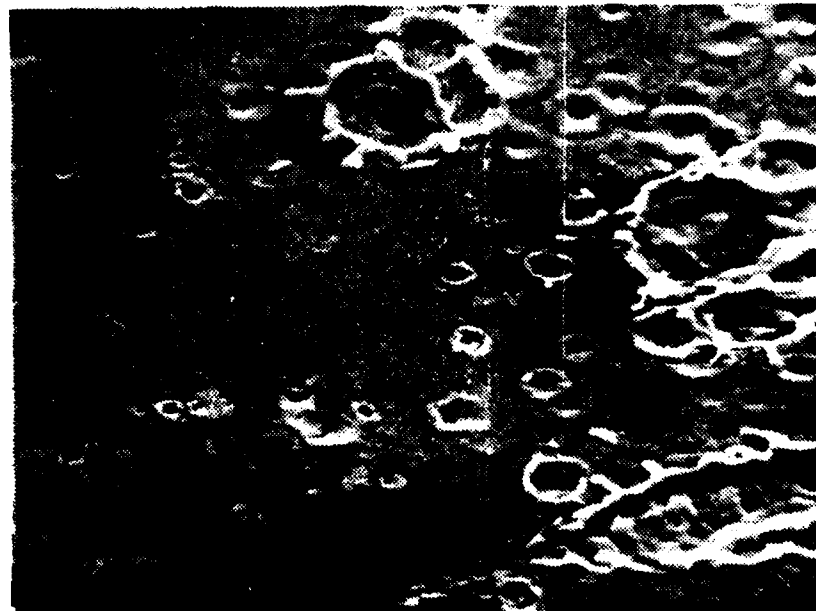


Figure 25. Polished 2024 Aluminum after Irradiation with  $400 \text{ MW/cm}^2$ , Edge of Melted Area, Typical Arcing over Unmelted Surface, SEM 460X.

cratering in the aluminum, with a crater size of 1 micron with rims up to 5 microns in diameter, and a crater density of approximately  $2 \times 10^6 \text{ cm}^{-2}$ . At the edges of the region of melted silicon and over the material outside the apparent radiation pattern, the surface of the silicon exhibited melted spots as photographed in Figure 25. These occurred in a band 50 microns wide with a density of about  $10^8 \text{ cm}^{-2}$ .

b. 1 Micron Silicon Coat

The thicker silicon coating exhibited extensive melting over essentially the entire irradiated area. It did not, however, melt through to the base aluminum at any point. The material appeared to have melted to a depth of about 0.5 micron, although this was not directly measured. Figures 27 and 28 are SEM photographs of typical areas of the exposed silicon and the structures prevalent throughout the exposed region. Figure 29 is a picture of material just outside the edge of the exposed region, and is typical of the entire border of the irradiated area. The density of the cratered areas in Figure 29 is approximately  $5 \times 10^7 \text{ cm}^{-2}$ , and crater size is about 0.1 micron.

6. SS-304 at  $10^9 \text{ W/cm}^2$

a. Unpolished SS-304

Samples irradiated at the higher power density evidenced surface melting and arcing over approximately 95% of the irradiated area. Arc crater size was about 1 micron

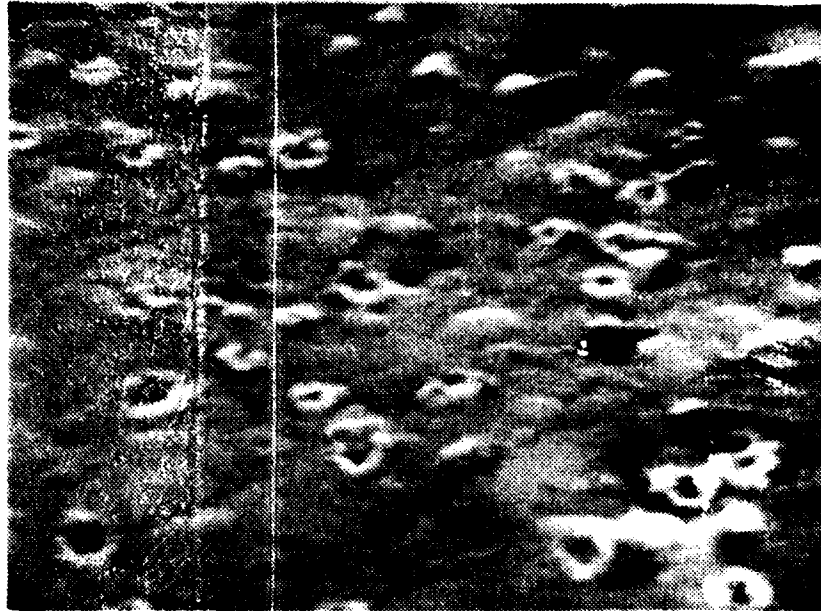


Figure 26. 0.2 Micron Silicon Coating over Polished 2024 Aluminum after Irradiation with  $400 \text{ MW/cm}^2$ , after Etching, Edge of Damage Area, SEM 10,800X.

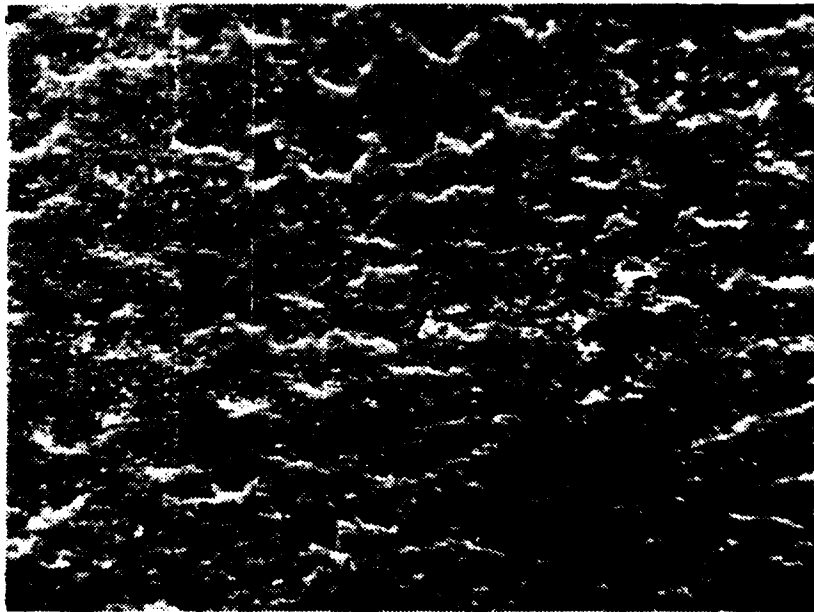


Figure 27. 1 Micron Silicon Coating over Polished 2024 Aluminum after Irradiation with  $400 \text{ MW/cm}^2$ , Center of Damage Area, SEM 1150X.

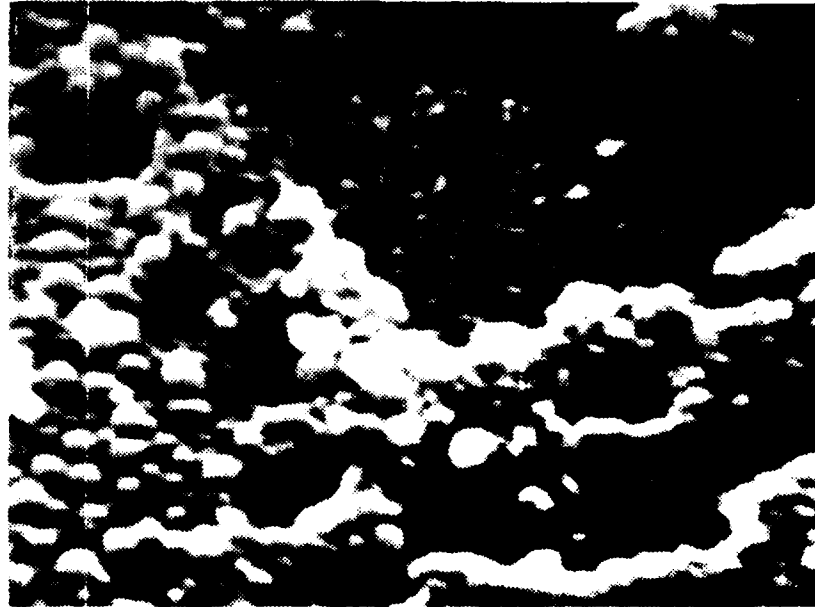


Figure 28. 1 Micron Silicon Coating over Polished 2024 Aluminum after Irradiation with  $400 \text{ MW/cm}^2$ , Near Edge of Irradiated Area, SEM 5600X.



Figure 29. 1 Micron Silicon Coating over Polished 2024 Aluminum after Irradiation with  $400 \text{ MW/cm}^2$ , Outside Edge of Irradiated Area, SEM 21,500X.

with rims to 5 microns, and appeared in a density of approximately  $5 \times 10^6 \text{ cm}^{-2}$ . Figures 30 and 31 picture a generally melted and cratered region and an enlargement of some typical craters respectively.

b. Polished SS-304

Surface melting and arcing appeared to cover approximately 90% of the surface of the polished sample at high power. Crater density in the heavily damaged regions was approximately  $3.4 \times 10^5 \text{ cm}^{-2}$ , and crater size ranged from 3 to 30 microns to the outer edge of the crater rim with central craters of about 1 micron. Figures 32 and 33 picture a generally melted and cratered region and a magnified crater respectively. There is evidence in the first photograph of craters occurring on top of older craters, and some of the smaller older craters may have been obscured by surface melting and subsequent cratering.

c. TiC-Coated SS-304

A series of TiC-coated targets was irradiated at power densities ranging from 300 to 1000 MW/cm<sup>2</sup>, and the targets were subsequently examined for surface damage. Table 16 gives the power densities achieved and Figures 34 through 36 picture typical damage for selected targets. Target damage at the lower power densities start with some flaking off of material in the center of the exposed area, and works out through regions of apparent melting and resolidification, cracking, and arcing, to undamaged material.

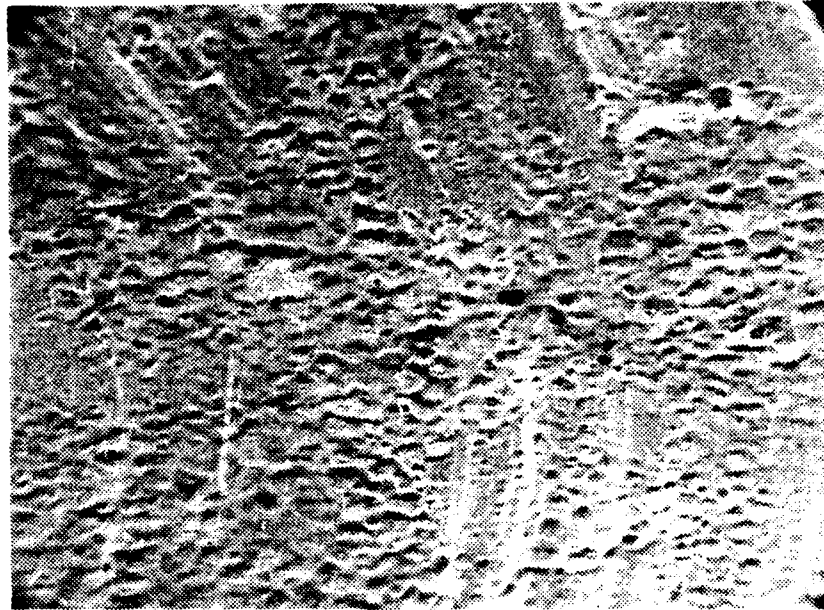


Figure 30. Unpolished SS-304 after Irradiation with 400 MW/cm<sup>2</sup>, SEM 235X



Figure 31. Unpolished SS-304 after Irradiation with 400 MW/cm<sup>2</sup>, SEM 2350X

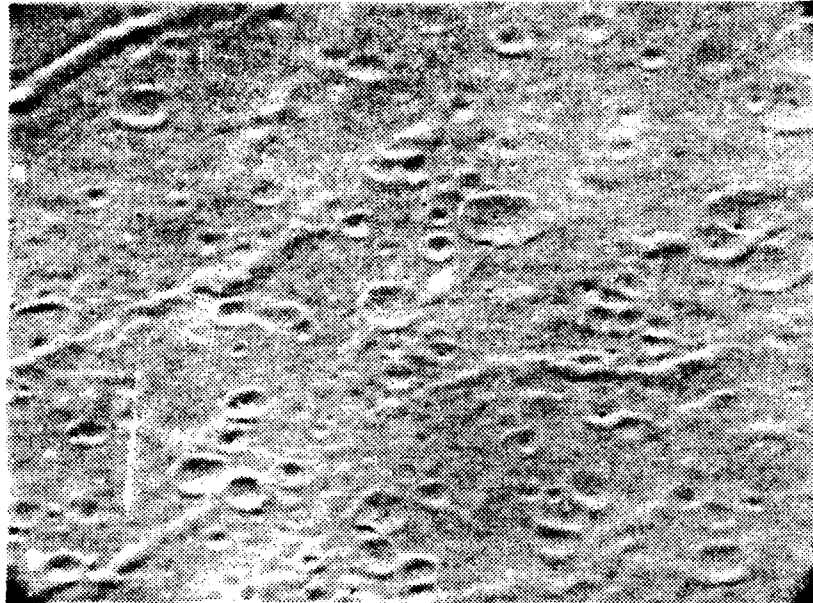


Figure 32. Polished SS-304 after Irradiation with  $400 \text{ MW/cm}^2$ , SEM 230X



Figure 33. Polished SS-304 after Irradiation with  $400 \text{ MW/cm}^2$ , SEM 1150X

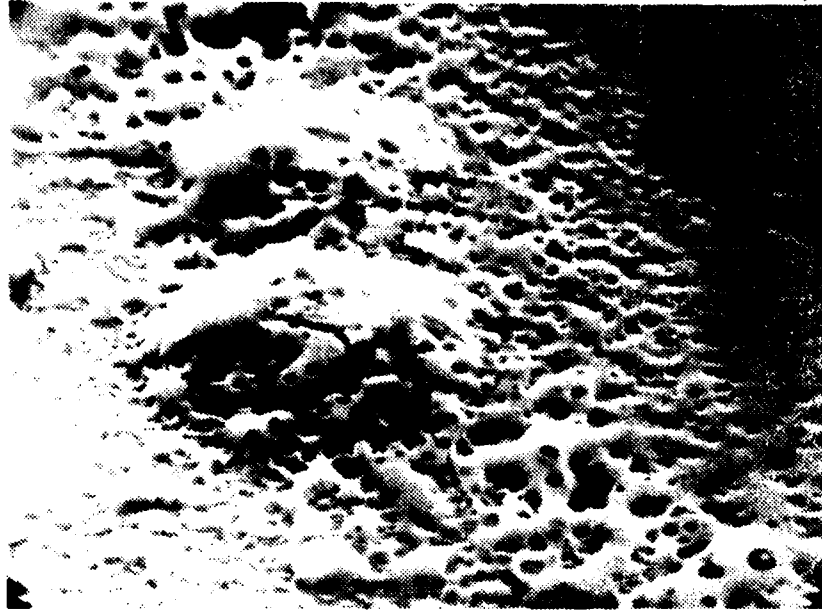


Figure 34. TiC Coated SS-304 after Irradiation with 300 MW/cm<sup>2</sup>, SEM 4800X.

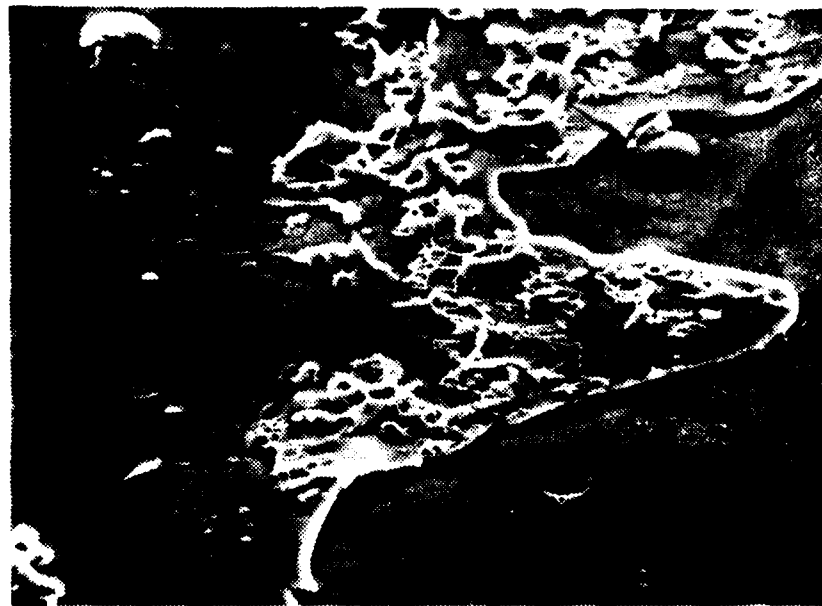


Figure 35. TiC Coated SS-304 after Irradiation with 872 MW/cm<sup>2</sup>, SEM 1200X.

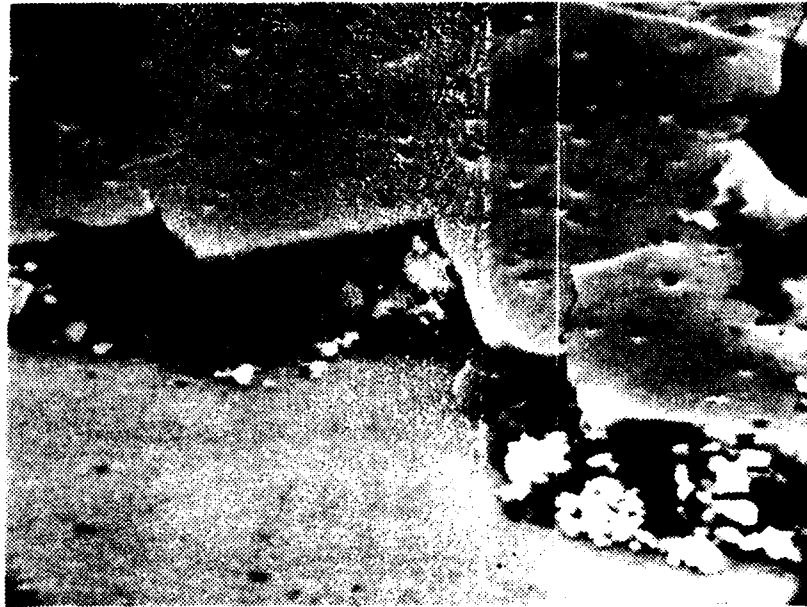


Figure 36. TiC Coated SS-304 after Irradiation with  $1096 \text{ MW/cm}^2$ , SEM 5400X.

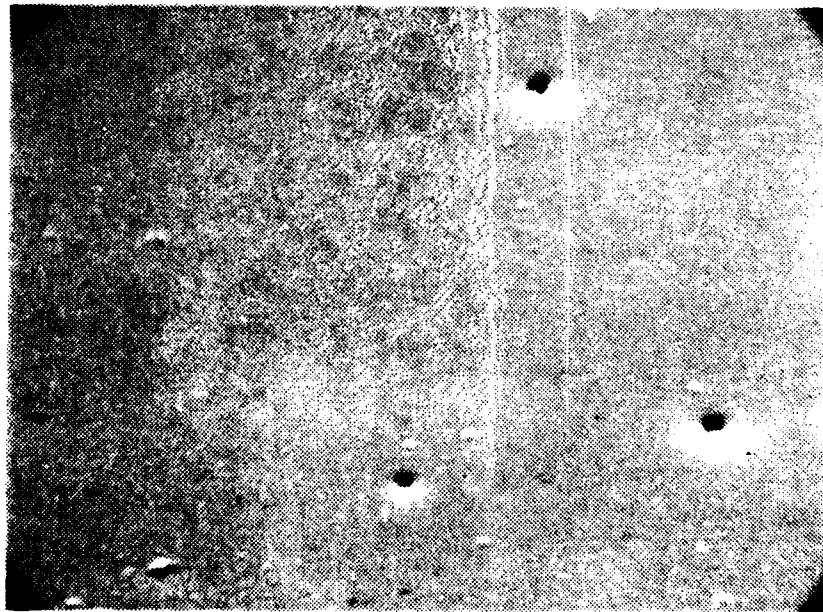


Figure 37. 1-2 Micron Silicon Coating over SS-304 before Irradiation, SEM 2100X.

Crater sizes range from 0.1 to 0.3 micron, with crater densities of approximately  $4.5 \times 10^2 \text{ cm}^{-2}$  in regions close to the melted material. At power densities near  $1000 \text{ MW/cm}^2$  the melted region at the edge of the beam does not appear, and the damaged region is essentially a layer peeled off the surface of the TiC. Along the edges of the removed TiC area, cracking and a very narrow band of arc craters appear. Figures 34 and 36 illustrate the difference.

d. 1-2 Micron Silicon Coat on SS-304

The silicon coating over SS-304 prior to irradiation is pictured in Figure 37. When irradiated the coating was damaged in much the same manner as was the 1 micron coating over aluminum. The same globules appear with size varying from the outer edges toward the center, and greater melting apparent in the center areas of the beam. Material has been removed from the surface in the center areas to an estimated depth of 0.5 micron. Figures 38, 39, and 40 picture typical surface effects at the edge of the damaged area, about 1 mm into the damaged region, and toward the center of the damaged area at a site exhibiting the most apparent surface melting and removal. Figure 41 pictures spheroid formation around the throat of pre-existent coating holes outside the irradiated area. Smallest spheroid size is about 0.1 micron.

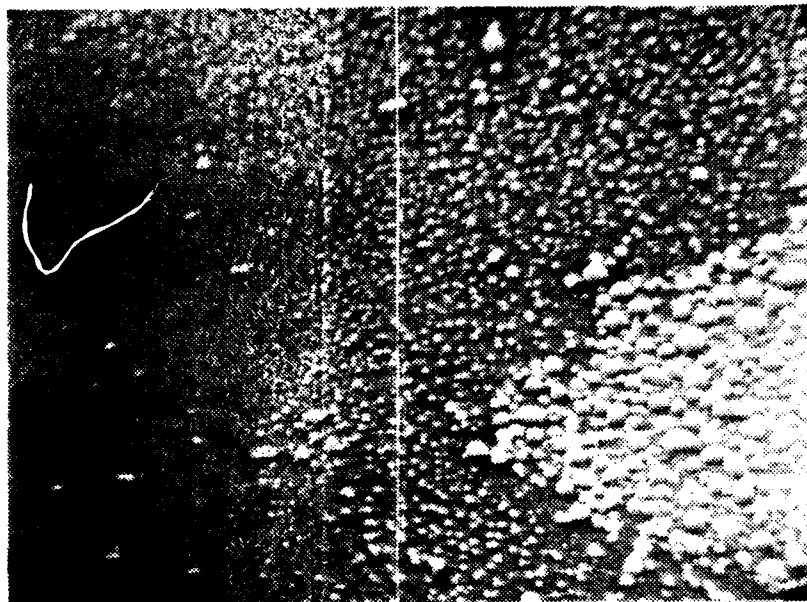


Figure 38. 1-2 Micron Silicon Coating over SS-304 after Irradiation with  $400 \text{ MW/cm}^2$ , Edge of Damage Area, SEM 2330X.

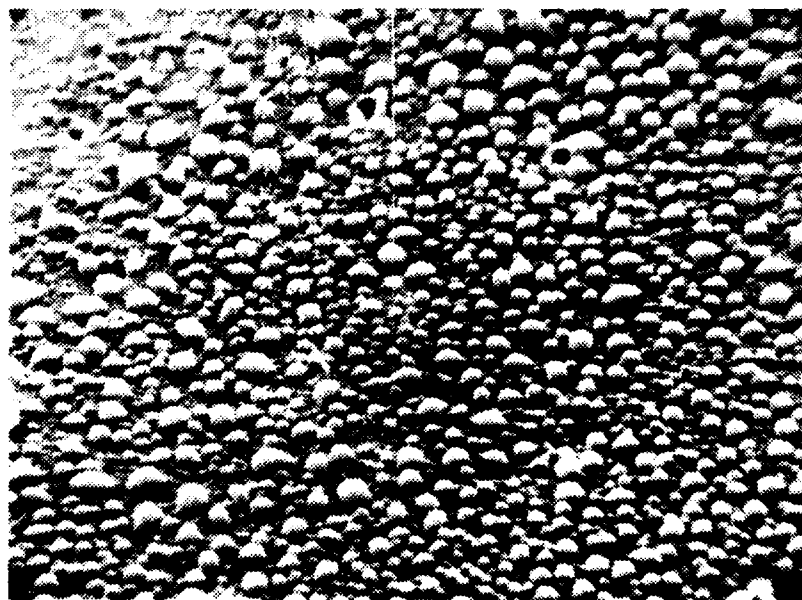


Figure 39. 1-2 Micron Silicon Coating over SS-304 after Irradiation with  $400 \text{ MW/cm}^2$ , Near Edge of Irradiated Area, SEM 2380X.

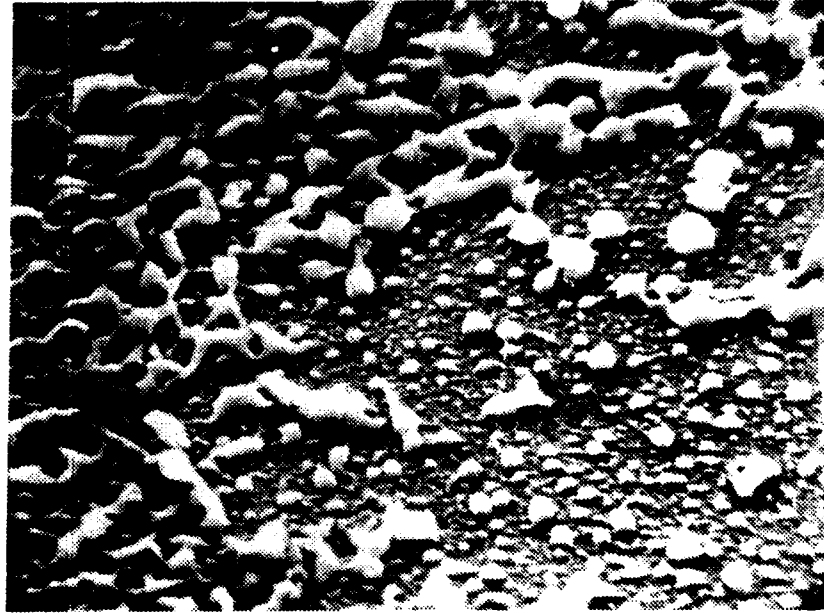


Figure 40. 1-2 Micron Silicon Coating over SS-304 after Irradiation with  $400 \text{ MW/cm}^2$ , Site of Greatest Apparent Melting, SEM 2300X.

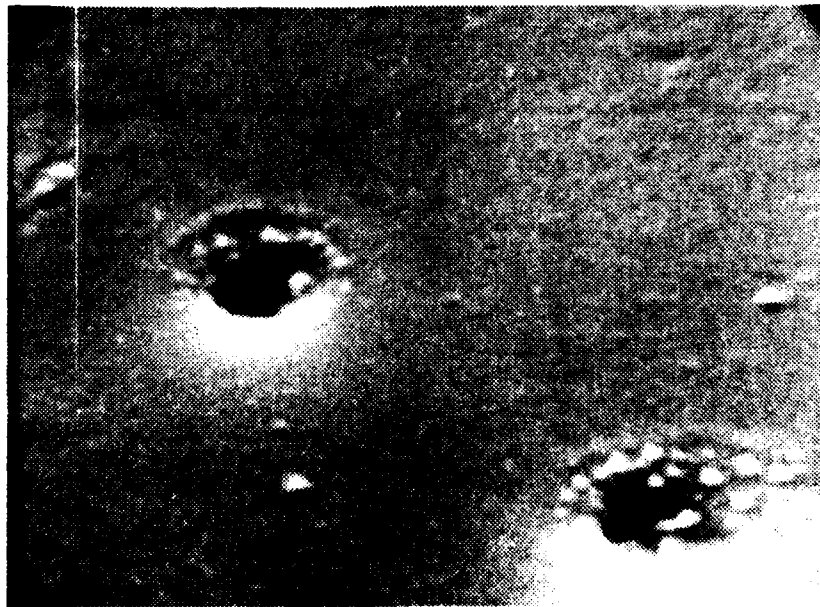


Figure 41. 1-2 Micron Silicon Coating over SS-304 after Irradiation with  $400 \text{ MW/cm}^2$ , Spheroid Formation Around Holes in Coating, SEM 5500X.

#### D. SAMPLE SPECULAR REFLECTIVITY

Specular reflectivity of the tested materials to 1.06 micron radiation was experimentally determined for typical samples of the surfaces used in this thesis. The values obtained differed from those tabulated for clean surfaces, but are considered useful for purposes of comparison. A reflectometer was not available to take the measurements, and the values for TiC and unpolished aluminum, which both showed some diffuse reflection, are probably the most inaccurate because of the method used. Table 17 lists the reflectivities that were measured for the target material used in this thesis.

## V. DISCUSSION OF RESULTS

### A. PLASMA ONSET

For the materials investigated, plasma onset irradiation power density is listed here in increasing order of magnitude:

<u>MATERIAL</u>	<u>ONSET POWER DENSITY (MW/cm<sup>2</sup>)</u>
Unpolished aluminum	4
TiC-coated SS-304	5.8
Polished aluminum coated with 0.2 micron silicon	6-7
Polished aluminum coated with 1 micron silicon	9-10
Polished aluminum	18

The following table lists the results of the reflectivity experiment of Section IV.D. in order of increasing reflectivity for the materials tested for plasma onset:

<u>MATERIAL</u>	<u>MEASURED REFLECTIVITY</u>
TiC-coated SS-304	0.444
Unpolished aluminum	0.514
Polished aluminum coated with 1 micron silicon	0.532
Polished aluminum coated with 0.2 micron silicon	0.594
Polished aluminum	0.855

Comparison of the results for aluminum in the two tables reveals that polished and unpolished samples retain their relative positions, but the ordering of the silicon-coated samples is reversed. The skin depth of silicon at room temperature is on the order of 10 microns for a wave length of 1.06 micron as mentioned in Section II.B.3, hence the effect of the silicon coat under the conditions of the reflectivity experiment would be to absorb the incident energy. This corresponds to the decrease in observed reflectivity. SEM investigation of the two silicon-coated surfaces revealed the 0.2 micron coating to have a less uniformly-coated surface, on which small spots were subsequently melted through. The thin irregular coating apparently provided spots for plasma onset to initiate, and then rapidly melted through. Beelby and Ulrich [Ref. 5] postulate that the formation of a seed plasma from gasses and other impurities adhering to the surface of a material is a primary mechanism responsible for plasma onset. The thin, irregular silicon coatings seem to have provided an enhanced environment for seed plasma formation when compared to polished aluminum. The optical and electrical properties of silicon change drastically as it is heated, until at its melting temperature it is essentially a metal, with a correspondingly short skin depth. The lower breakdown power density for the thinner coating arises from its exposure to a combination of incident and reflected laser

radiation of higher intensity due to smaller coating thickness with lower total absorption. The result is an increased rate of heating of the silicon.

The experimental limitations of the investigation include the accuracy of measurement of incident energy, determination of beam spot size on the target, the assumption of a gaussian beam, and the use of the polaroid camera to detect plasma. Of these, the assumption of a gaussian beam provides the least predictable and largest magnitude error, as the existence of beam hot spots produced regions of power density much higher than the calculated value. Use of the polaroid as the plasma detection device probably created the second largest source of error, as the glow observed in the photograph may have been produced by some mechanism such as incandescent glow in cases where no post-irradiation surface damage was observed. This particular limitation applied only to TiC.

In conclusion, plasma onset in aluminum appears to be extremely dependent upon reflectivity, with a secondary dependence on freedom of the surface from adhering material. For silicon-coated aluminum, onset is a more complicated function of the thickness of the coating, its regularity, and the reflectivity of the composite. For coatings of equal surface regularity thicker than 10 microns, plasma onset power density should be almost a constant. For

comparison of different materials, the most significant indication of plasma onset power density is surface reflectivity.

## B. THERMAL COUPLING

### 1. 2024 Aluminum

Thermal coupling results for the different coated and uncoated aluminum samples tested are summarized in the following table:

<u>SURFACE</u>	<u>POWER DENSITY RANGE (MW/cm<sup>2</sup>)</u>	<u>AVERAGE COUPLING COEFFICIENT</u>
Unpolished aluminum	320-462	0.138
Polished aluminum	335-483	0.00838
0.2 micron silicon coat	339-429	0.0175
1 micron silicon coat	316-495	0.00718

Comparison of the results for the two uncoated aluminum samples indicates that the coupling coefficient difference correlates well with the reflectivity difference listed in Section V.A., above. This observation does not apply to the aluminum to silicon coating comparisons, however. Examination of the two aluminum surfaces after irradiation revealed that while approximately 90% of the unpolished surface within the beam spot had apparently experienced surface melting and unipolar arcing, only about 60% of the polished surface was similarly damaged.

For both types of silicon-coated surfaces, approximately 95% of the irradiated area exhibited surface damage effects.

SEM examination of the damaged areas of the two aluminum targets revealed essentially identical damage over the areas involved in melting and arcing, including crater densities of the same order of magnitude. A similar examination of the two coated targets revealed very dissimilar surface damage. The 1 micron silicon coat appeared to have been partially melted and vaporized with material removed to a depth of about 0.5 micron. The surface of the remaining material apparently had melted and resolidified in formations promoted by surface tension. The remaining 0.5 micron appeared undamaged, but exhibited a very rough and uneven surface indicating it may also have experienced some melting. In contrast, the 0.2 micron coat was completely removed from the aluminum, and the underlying aluminum exhibited apparent melting and arcing. To confirm the complete removal of silicon from the laser irradiation spot, the target was lightly etched with a solution of HF and distilled water for 15 seconds to outline and highlight any remaining silicon particles. None were revealed during subsequent SEM examination.

The coupling coefficient difference between the polished and unpolished aluminum samples correlates closely with the difference in percentage of irradiated surface

involved in the melting and arcing. The coupling coefficient ratio for unpolished to polished was 1.69, while the corresponding area percentage ratio was 1.5. Surface breakdown involvement is, in turn, a function of the surface reflectivity and the energy density profile of the laser beam. The coupling coefficient is considered to be predominately a function of the percentage of surface breakdown.

The difference between the coupling coefficients for the silicon coatings does not yield to the above analysis. In this case the interaction processes are significantly different. Baeri et. al. [Ref. 24] calculated the temperature response of silicon to a 20 nanosec pulse of a Q-switched ruby laser with an energy density of about  $1.8 \text{ J/cm}^2$ . The results indicate that the surface heats to a temperature above the melting point within the first 10 nsec of the laser pulse, and that melting of the silicon takes place down to a depth of about 0.25 microns. This assumes all the energy is coupled to the target.

Consideration of the melting and vaporization observed during this investigation leads to the following reasoning for the observed thermal coupling differences. First, in the case of the 0.2 micron silicon coat, about 0.2 joules would be required to heat, melt and vaporize the coating. The aluminum surface would then be exposed to the boiling temperature of silicon, 3543 Kelvin. This is above the boiling temperature of aluminum, however, and

cooling by aluminum sublimation or evaporation would be occurring simultaneously to the aluminum boiling point, 2753 Kelvin. The uncoated aluminum by comparison would have some areas at the melting temperature of aluminum, and some areas at temperatures up to its boiling point. In the case of the thinly-coated silicon, the coating provides a greater heat source than exists with uncoated aluminum.

Considering the 1 micron coatings next, the energy required to vaporize the thickness of silicon which appeared to have been removed from the target was about 0.6 joules. The temperature at the silicon surface would then have been the melting temperature of silicon, 1683 Kelvin, with some areas heated to the boiling temperature. The thermal conductivity of silicon is about 27% lower than that of aluminum, resulting in slower transport of thermal energy to the aluminum, and longer times for radial thermal transport and black body reradiation. The extremely large quantity of material being vaporized from this coating and injected into the plasma contributes to a very dense plasma, and may result in energy being cut off from the incident laser energy as the plasma reaches critical density. These qualitative arguments delineate the apparent mechanisms leading to the differences in observed coupling values. It must also be noted that the reasoning used here would not necessarily apply in the case of repeated pulses.

## 2. SS-304

The thermal coupling results for the coated and uncoated SS-304 samples tested are summarized in the following table:

<u>SURFACE</u>	<u>POWER DENSITY RANGE (MW/cm<sup>2</sup>)</u>	<u>AVERAGE COUPLING COEFFICIENT</u>
Unpolished SS-304	363-458	0.0188
Polished SS-304	318-461	0.0193
1-2 micron silicon coat on SS-304	368-433	0.0150

The coupling coefficients for polished and unpolished SS-304 are essentially identical within the accuracy of the investigation. SEM examination of the two different surfaces after irradiation revealed the same damage on both surfaces, i.e., melting and cratering. However, the unpolished material appears much more uneven and has more spots of very little damage. Arc crater density is about an order of magnitude higher on the unpolished material, but surface melting is more evenly spread over the entire surface of the polished material. On the macroscopic level, surface damage appeared to involve about 90% of the polished surface irradiated, and about 95% of the unpolished surface. As indicated by the aluminum results in the previous section, thermal coupling is apparently predominately a function of the percent of surface breakdown.

The silicon coating applied to the SS-304 had a much smoother finish than that applied to the aluminum. However, SEM examination after irradiation revealed essentially the same damage as exhibited by the silicon coating on aluminum. The thermal coupling reduction mechanism in this case must rest almost entirely with the energy removed in vaporization of the silicon, and the cutoff of incident laser energy by critical density plasma. The other mechanisms mentioned for the coated aluminum targets would be ineffective here, as the thermal conductivity of SS-304 is an order of magnitude lower than that of silicon, and the melting temperatures of the materials are essentially identical.

### 3. Experimental Limitations

The experimental factors limiting the accuracy of the thermal coupling results include: the assumption of one-dimensional heat conduction, the accuracy of the temperature rise measurement, the accuracy of beam energy measurement, the accuracy of spot size measurement, the limited number of silicon-coated samples available for both SS-304 and aluminum, and the treatment of thermal conduction coefficients as constants while they are in fact temperature dependent.

## C. SURFACE DAMAGE EFFECTS

### 1. 2024 Aluminum

Both the polished and unpolished surfaces exhibited essentially identical damage patterns, i.e., surface melting

and arcing, at both onset and high power densities. Melting took place in the areas of the beam where energy intensity was sufficiently high, and arcing took place in both the melted areas and the nearby unmelted areas. Observed arcs were of the size and form expected, and are reasonably explained by the arcing model already discussed. Minimum plasma densities compatible with the 1 micron craters observed are on the order of  $5 \times 10^{16} \text{ cm}^{-3}$ . This number is determined using Equation 10, assuming crater diameter must be on the order of 10 times the Debye length and  $kT_e$  is 10 ev. This should be compared with the critical plasma density of  $10^{21} \text{ cm}^{-3}$  obtained in section II.B.2.

## 2. SS-304

Like the aluminum tested, both the polished and unpolished SS-304 experienced very similar melting and arcing damage. Melting again occurred only in the high intensity areas of the beam, while arcing occurred over both melted and unmelted material. The smooth polished surface displayed the arc spots much more clearly than the unpolished material. However, crater sizes in both samples appear to be essentially the same. The crater size and distribution appear consistent with the arcing model previously expressed. Plasma density consistent with the observed 1 micron crater size is of the order of  $5 \times 10^{16} \text{ cm}^{-3}$ .

### 3. Silicon Coatings

Damage to silicon coatings was of a more complicated nature. As mentioned in section II.B.3.a., at room temperature the absorption length in silicon for 1.06 micron radiation is on the order of 10 microns, far greater than the thickness of any of the films tested. Under the influence of the incident laser pulse, however, the silicon surface heats and starts to melt within a few nanoseconds [Ref. 24]. Once heating commences, the electrical properties of silicon change rapidly [Ref. 16: p. 84], until at the melting point silicon is essentially a metal [Ref. 25], with a skin depth on the order of 260 angstroms. Baeri et. al. [Ref. 24] calculated the depth of melting for silicon exposed to a 20 nanosecond pulse from a Q-switched ruby laser with an energy density of about  $1.8 \text{ J/cm}^2$  to be about 0.25 microns. This result assumed all energy coupled to the target. Their further calculations predicted increasing melting to depths of greater than a micron as energy density is increased for pulse lengths between 20 and 100 nanoseconds, and wavelengths between 0.694 and 1.06 microns.

Examination of targets exposed to energy densities of from 6 to  $11 \text{ J/cm}^2$  revealed melting and evaporation to depths of up to 0.5 micron, with possible limited melting beyond that depth. However, melting was never found through the entire 1 micron thickness of the coating. Baeri et. al.

[Ref. 24] indicate melting to 1 micron should occur for coupled energies on the order of  $3 \text{ J/cm}^2$ . Apparently material vaporization and plasma formation interfere with the coupling of energy to the target and the melting process.

0.2 micron silicon-coated aluminum targets displayed spots of surface melting at onset power density, with some indication of melting extending through the entire coating thickness. Most of the melted regions have dimensions on the order of 1 micron or greater and probably indicate surface melting under beam hot spots. Many others, however, have dimensions of less than 1 micron, and are considered to be unipolar arc craters. Considering the changes in material properties that silicon experiences on heating, the observed surface damage pattern results from heating to less than melting temperature of the irradiated surface, melting/vaporization in beam hot spots, followed by unipolar arcing under the resultant plasma in areas close to the plasma formation spots. Initial plasma formation is assisted by the irregularity of the surface, and subsequent formation of unipolar arcs is facilitated by silicon's resistivity having been lowered by heating, and the electric field enhancement provided by the surface irregularities.

At high power densities the silicon completely melted and vaporized in the center areas of the target, but damage patterns similar to the onset pattern were found

in a band around the removed material. The deposited energy melted and vaporized the major portion of the irradiated area, while the resultant plasma interacted with the now uncovered aluminum and the remaining silicon, forming unipolar arcs.

The thicker silicon coating on aluminum interacted in a very similar fashion, but the characteristic surface damage pattern consisted of small spherical globules of silicon rather than holes. Plasma onset samples displayed concentrated regions of spheres in areas of greatest beam intensity, with a few small areas of material melted and removed to an approximate depth of 0.5 micron. Typical spheroid size was 0.8 micron, while material was removed from spots of about 10 micron diameter or less. Silicon melting and vaporization was a direct effect of the laser radiation in the areas of dense globules and where the 10 micron chips were removed. Bordering the regions of concentrated spheres were bands of smaller, less numerous spheres and some crater-like formations. These less-densely packed and generally smaller features were the result of surface heating followed by unipolar arcing under the expanding plasma.

There is no direct evidence of unipolar arcing occurring over the melted regions of either the thick or thin coatings. However, the existence of craters in the bordering regions and the electrical properties of silicon

on melting suggest that the conditions were appropriate for arcing to occur. A rough calculation of the time required for the spheroids to form, using the surface tension and speed of sound in liquid silicon, and an approximation of the mass in an average spheroid, yields an average time on the order of 1 microsecond. This suggests that the liquid persists longer than the plasma, and any evidence of arcing would be obliterated.

The silicon coatings over SS-304 had a much smoother surface and did not respond exactly as the aluminum coatings did. The coatings over SS-304 were not tested at plasma onset. At the higher power density levels, the characteristic melting and vaporization of material occurred in the high intensity areas of the beam, with melting and spheroid formation pervading the rest of the irradiated area. At the edge of the irradiated area there existed a very sharp border of very small dispersed spheroids outside the large solidly packed spheroids marking the irradiated area. In areas well away from the irradiated area, around the throats of vortice-shaped holes in the as-applied coating, similar areas of small dispersed spheroids exist. The existence of this same damage pattern in two areas separated by apparently undamaged material leads to the conclusion that the damage is a surface-plasma interaction effect. The curvature of the surface in the hole throat would provide

an electric field enhancement feature, and suggests unipolar arcing as the damage mechanism. The similarity of the damage bordering the irradiation area suggests that the same damage mechanism is present there.

#### 4. TiC Coating

Surface damage to TiC-coated SS-304 was investigated for samples exposed to plasma onset and to a range of power densities from 271 to 1096 MW/cm<sup>2</sup>. Observed surface damage varied greatly across the range, from no observed damage at plasma onset, to various combinations of flaking, melting, and arcing at higher power densities. At power densities in the vicinity of 300 MW/cm<sup>2</sup> the coating exhibited flaking, melting, and apparent arc craters in three distinct regions. The flaking occurred in the center of the irradiated area, under the apparent area of most intense radiation. The melting borders the flaked region, and is characterized by a honeycombed surface, apparently promoted by surface tension. This region also has extensive surface cracking, and small crater pockmarks exist in the melted and resolidified surface. The final region of damage borders the melted area away from the flaked material. This region is characterized by some surface cracking and many tiny craters. Typical crater size was 0.1 to 0.3 micron. At higher power densities the flaking and cratering persist, although their areas change, but the melted region varies in area, then disappears. On the sample exposed to 1.096 GW/cm<sup>2</sup>

the flaked region pervades almost all of the irradiated area, and is surrounded by a very narrow region of cracked and cratered material, with no melted material evident.

The proposed surface response to the laser beam leading to the observed damage is melting and vaporization of some material in the most intense part of the beam, with thermal forces then blowing flakes off the surface. Figure 42 is a polaroid photograph of TiC-coated SS-304 during exposure to a  $75 \text{ MW/cm}^2$  laser pulse. The streaks in the photograph show the coating being blown off the target surface on a path normal to the surface. The laser pulse was incident on the target at 30 degrees from the target normal in the plane of the photograph, and is not seen because of filtering. Surrounding areas under less intense radiation are simultaneously experiencing some melting and vaporization with unipolar arcing occurring under the resultant plasma. At the edge of the melt area the surface still experiences some heating, and this region also supports unipolar arc craters under the expanding plasma. The narrowness of the band of arcing in the high power shots where melting is not seen indicates that a certain amount of preheating is needed before the TiC becomes arc susceptible. The size of the arc craters observed makes it extremely unlikely that arc damage would have been found on the onset target samples, even if it occurred.

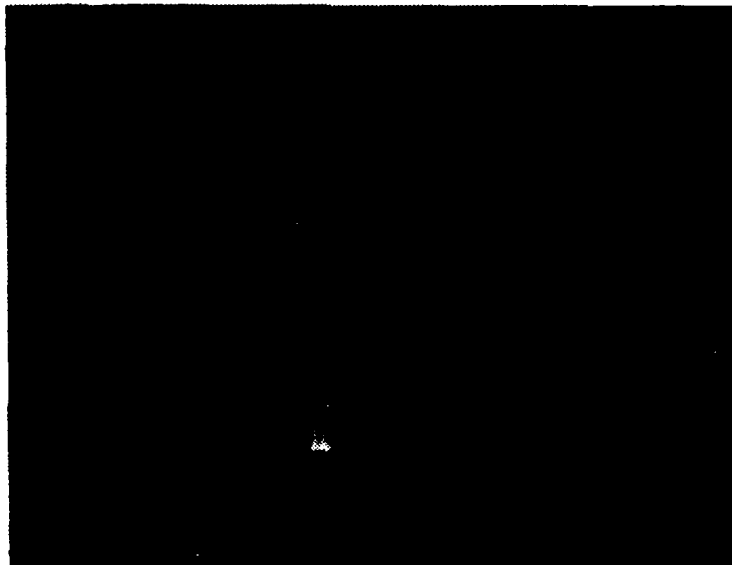


Figure 42. TiC Coated SS-304 Irradiated with  $75 \text{ MW/cm}^2$ ,  
Streaks Caused by Coating Blowing off  
Normal to Target Surface.

## 5. Crater Size

The small size observed for craters on silicon and TiC may be explained by considering the characteristics of the materials, and the electric field strengths available at the plasma-surface interface. Qualitatively, if the electric field is considered to be caused by a plasma sheath effect, then  $E = V_f/\lambda_D$ . Hence for plasmas of similar characteristics, i.e., temperature and density,  $E$  is essentially independent of material type and can be considered constant from material to material. Assuming a constant  $E$ , the high resistivity of silicon would require the radially inward surface return currents to converge to a smaller cathode spot diameter to achieve sufficient current density to vaporize and ionize the material at the cathode arc spot. Similarly, for TiC, because it has a higher resistivity than most metals and is an extremely stable compound with a very high melting temperature, high current densities would be required, and could be achieved only by the surface return current converging to a smaller arc spot.

If ohmic heating is used as the primary power source for the vaporization of the arc spot, power may be written as

$$P_R = I^2 R. \quad (11)$$

Assuming cylindrical symmetry, a constant crater depth  $\Delta z$ , and negligible axial current into the initial crater spot,

total current is a function of current density and crater radius  $r$ ,

$$I = j(r) 2 \pi r \Delta z. \quad (12)$$

Here it is assumed for a radially converging current that  $j(r)$  is an inverse function of radius. The resistance  $R$  of the material is a function of resistivity  $\gamma$ , the cross-sectional area and the length of the conductor  $\ell$ :

$$R = \frac{\gamma \ell}{2 \pi r \Delta z} \quad (13)$$

Power per unit volume is a more useful quantity than power, and crater volume is the most useful volume increment:

$$V = \pi r^2 \Delta z \quad (14)$$

Equations 11 through 14 yield a relationship for power density:

$$P_R/V = \frac{2j^2(r)\gamma\ell}{r} \propto \frac{1}{r^3} \quad (15)$$

Solving equation 15 for  $j^2(r)$  and assuming  $r=\ell$  one finds

$$j^2(r) = \frac{1}{2\gamma} \left( \frac{P_R}{V} \right) \quad (16)$$

Taking  $P_R$  as energy to vaporize per unit time and assuming a time scale of 10 nanoseconds for a crater to form, current

density is found to be on the order of  $10^8$  amps/cm<sup>2</sup> for silicon. This number was found using the melting point resistivity of silicon. It is estimated that a more detailed calculation would yield a smaller figure by about an order of magnitude due to the high resistivity of silicon at room temperature. The calculated current density of  $10^8$  amps/cm<sup>2</sup> is in the range of values proposed by Ecker [Ref. 31].

If the radial electric field is assumed to be the same between two materials, then from Ohm's law the current density at a certain radius will vary inversely with the resistivity  $\gamma$ . Since current density appears to the second power, power density will drop if resistivity increases. Therefore, a material with a higher resistivity should require a smaller crater radius to achieve the power density to vaporize the material at the arc spot. This assumes that the power density to vaporize the arc spot is essentially equal for materials compared in this manner.

It is noteworthy that  $\Delta z$  does not appear in equations 15 or 16. This is a direct result of the assumption that initial crater depth and surface current depth are approximately equal, a requirement if ohmic heating is the principal power source. A relationship between  $\Delta z$  and  $r$  can be developed by comparing total cathode emission current out of the cathode spot surface  $j_s \pi r^2$  where  $j_s$  is the surface current density, to total return current through the surface layer

of the material into the cathode spot, equation 12. The result is

$$\Delta z = A \left( \frac{r}{2} \right) \quad (17)$$

In this relationship, the surface current depth,  $\Delta z$ , is a property of the material and the proportionality constant  $A$  is the ratio of the current density out of the cathode spot to the radial return current density evaluated at the crater radius.  $A$  is considered to be on the order of one.

In the case of silicon the large resistivity and correspondingly small current density would easily result in a crater size one or two orders of magnitude smaller than that observed on metals. Actual size would depend on actual resistivity, which in turn depends on temperature.

In the case of TiC, the resistivity is almost two orders of magnitude larger than 2024 aluminum, and the power density to vaporize is considered to be significantly higher because of its chemical stability and high melting temperature. Smaller crater size would again provide the needed power density to vaporize the material for running the unipolar arc.

#### D. SPECULAR REFLECTIVITY

The results of this section, considered within categories by base metal, are self-consistent, and the values for aluminum compare well with literature values for clean

surfaces [Ref. 17: p. 8]. The decrease in reflectivity between the polished metals and the polished metals coated with silicon may be explained by considering the effect of the coating.

The silicon coatings over aluminum were lumpy and irregular, and had two effects on specular reflectivity, i.e., absorption and diffuse reflection. Each coating should contribute about equally to diffuse reflection of the incident light, but the thicker coating should contribute more to absorption. This is indeed the case as attested to by the lower reflectivity reading of the thicker coating. The silicon coat over SS-304 was very smooth and even, and should decrease reflectivity only by its absorption. This is apparent in the small decrease in measured reflectivity from uncoated to coated SS-304.

Taking the reflectivity and absorption length of silicon at 1.06 micron incident radiation as 0.3 and 10 microns, respectively [Ref. 17: p. 9], reflectivity for the 1 micron silicon-coated SS-304 may be computed as follows:

$$R = R_{si} + \left(1 - R_{si}\right) e^{-\frac{2x}{\ell}} R_{ss} \quad (18)$$

Here R refers to reflectivity of the coated target, the subscripts refer to reflectivity of the silicon (si), or SS-304 (ss),  $\ell$  in the exponent is the absorption length, and x is the path length. Using this equation and assuming

the reflectivity of SS-304 is the value measured for the uncoated material, a value of 0.744 is obtained. This compares with the measured value of 0.725.

The lower values of reflectivity for TiC and the two unpolished materials may be attributed to the more irregular character of their surfaces resulting in more diffuse reflections.

## VI. SUMMARY AND CONCLUSIONS

This study was concerned with the thermal coupling and plasma-induced surface damage of various target materials in a vacuum when exposed to a Q-switched 20 nanosecond laser pulse. The preceding sections have discussed the established theory involving the phenomena under investigation, and then described the experimental results obtained. In reviewing the results and their meaning, several conclusions can be made concerning what is occurring during the laser-surface interaction.

At low power densities, plasma onset was examined closely for TiC-coated SS-304 foil and AL-2024 in polished, unpolished, and silicon-coated forms. In comparing the polished and unpolished aluminum, there is a direct correlation between reflectivity and power density required for plasma onset. This has obvious implications in the real world, where a highly-polished target would require a higher power density for plasma initiation than an unpolished target. As an outgrowth of this argument, the freedom of the surface from irregularities and adhering impurities will lead to an increase in the threshold power density for plasma onset. In this area the results of this thesis expand and verify the results of Beelby and Ulrich [Ref. 5].

TiC-coated stainless steel exhibited no apparent surface damage at low power densities even though a plasma was formed. This is in contrast to the aluminum which displayed unipolar arcing damage and melting at plasma onset power densities.

The silicon-coated aluminum exhibited behavior at low power densities unlike that of uncoated aluminum. The 1 micron silicon coating, which displayed a lower reflectivity than the 0.2 micron coating, actually had a higher breakdown threshold value. As explained in section V. A., the conclusion is that plasma onset power density is a function of coating thickness and smoothness.

At higher power densities, thermal coupling and surface damage effects were examined in order to determine the damage mechanisms which occur during a laser-surface interaction, and how the damage is related to thermal coupling of energy to the target. It was concluded that thermal coupling is predominately a function of the percent of irradiated surface experiencing breakdown for uncoated materials. In the case of uncoated aluminum, the lower percent of surface damage for the polished samples is due to higher reflectivity, which leads to a lower coupling of energy to the target. In the cases of uncoated SS-304, it must be concluded that thermal coupling is not a function of surface finish. Both polished and unpolished SS-304 exhibited essentially equivalent percentages of surface

damage and equal thermal coupling coefficients. The data for stainless steel obtained in this thesis closely agree with that published by Metheny [Ref. 6].

For silicon-coated targets, the case is again explained by a different physical model. The conclusion here is that a coating of sufficient thickness will be able to absorb the incident laser energy without melting through to the base material. The thermal coupling retardation mechanism is surface ablation and reflection of incident energy by the dense plasma.

At high power densities, observations of surface damage by unipolar arcing to SS-304 and Al-2024 are consistent with the results of Beelby and Ulrich [Ref. 5] and Ryan and Shedd [Ref. 3]. Unipolar arcing was also observed on silicon-coated aluminum, with arc craters an order of magnitude smaller and crater density an order of magnitude larger than the uncoated aluminum. Arc craters were not seen on silicon-coated SS-304. However, the size and distribution of the surface damage features (spheroids) strongly suggest that unipolar arcing was present.

Unipolar arcing was also observed on TiC-coated SS-304, contrary to previously reported results. The crater size was an order of magnitude smaller than that observed on uncoated SS-304, while crater density was 2 orders of magnitude larger.

Observation of differences in crater sizes for different materials led to the conclusion that crater size is a function of material resistivity and the power per unit volume required to vaporize the material. A model is proposed to describe the relationship.

## VII. RECOMMENDATIONS

Because of the discovery of unipolar arc craters in TiC-coated SS-304, it is recommended that unipolar arcing and thermal coupling be further investigated for this material. Additionally, silicon-coated SS-304 should also be tested for unipolar arcing to confirm the strong evidence found in this thesis that arcing is occurring. Determination should be made of the time scale of the partial flaking of the TiC coating, and of the plasma densities and temperatures close to the laser impact area for both coatings.

Due to the insignificant difference in thermal coupling between polished and unpolished SS-304, more data should be obtained and a closer examination made of physical properties or mechanisms which might explain this observation.

In addition to the metal targets examined in this thesis, it is highly recommended that a solid dielectric be investigated to obtain plasma formation and thermal coupling data. A comparison of data and physical properties with that provided in this thesis for metals and silicon might provide greater insight into what physical mechanisms are operative in laser-surface interactions.

Finally, it is considered important for reliable and meaningful data that thin targets be used when investigating thermal coupling. Not only will temperature measurements be

more accurate, but also a one-dimensional heat conduction problem will be assured.

APPENDIX A

PHYSICAL PROPERTIES OF SELECTED MATERIALS

	TiC	Al 2024 <sup>1</sup>	SS 304 <sup>2</sup>	Si
Density (g/cm <sup>3</sup> ) @ 20°C	4.25	2.77	8.0	2.34
Melting Range (°C)	3140	502-638	1400-1450	1410
Boiling Point (°C)	4300	2480	2700	3270
Electrical Conductivity (Ω/cm) @ 20°C	9.5 x 10 <sup>3</sup>	2.94 x 10 <sup>5</sup>	1.4 x 10 <sup>5</sup>	9.5 x 10 <sup>-6</sup> ; (1.33 x 10 <sup>4</sup> @ 1410 °C)
Thermal Conductivity (W/cm-K)	0.172 (@ 25°C)	1.90 (@ 25°C)	0.162 (@ 100°C)	1.385 (0-100°C)
Thermal Diffusivity (cm <sup>2</sup> /S)	0.073	0.784	0.041	0.873
Specific Heat (J/g-K) @ 20°C	0.552 <sup>3</sup>	0.875	0.50	0.678
Latent Heat of Fusion (KJ/mol)	-	10.47 (pure Al)	15.2 (Pure Fe)	50.66
Latent Heat of Vaporization (KJ/mol)	-	291.4 (pure Al)	340.4 (Pure Fe)	384.8
Reference	27,28	26,27, 30	26,27, 29	27,29 16(p. 84)

- Notes: 1. Al 2024 composition: 93.5% Al, 4.4% Cu, 1.5% Mg, 0.6% Mn.  
 2. SS 304 composition: 66-71% Fe, 18-20% Cr, 8-10.5% Ni, 2% Mn, 1% Si, 0.08% C, .045% P, .03% S.  
 3. Computed at 20°C from  $C_p = 4.1868 (11.85 + 0.8 \times 10^{-3} T - 3.58 \times 10^{-5} T^{-2}) \text{ J/K}^{\text{mol}}$ .

APPENDIX B

TABLES

Table 1. Time to Reach Boiling Temperature for Target Material.

<u>Material</u>	<u>Time (nanoseconds)</u>
TiC	0.0362
Al 2024	0.1346
SS 304	0.0227
Si	0.0759

Table 2. Skin Depth for Target Material.

<u>Material</u>	$\delta(\text{\AA})$
TiC	306.9
Al 2024	55.2
SS 304	80.0
Si (1410°C)	259.4

Table 3. Diffusivity Times for Target Material.

<u>Material</u>	<u>d(cm)</u>	<u><math>\kappa(\text{cm}^2/\text{s})</math></u>	<u><math>r_o(\text{cm})</math></u>	<u><math>\tau_d(\text{sec})</math></u>	<u><math>\tau_r(\text{sec})</math></u>
AL 2024	0.19	0.784	0.275	0.0115	0.0241
SS 304	0.12954	0.041	0.0275	0.1023	0.4611

Table 4. Plasma Onset Data for TiC-coated SS-304 Foil.

<u>TGT#</u>	<u>Power Density (MW/cm<sup>2</sup>)</u>	<u>Plasma Evident</u>	<u>Surface Damage</u>
5	108	YES	YES
6	113	YES	YES
7	103	YES	YES
8	67.7	YES	YES
9	71.9	YES	YES
10	64.8	YES	YES
11	74.7	YES	YES
12	70.1	YES	YES
13	20.4	YES	NO
14	10.8	NO	NO
15	13.4	YES (DIM)	NO
16	10.6	YES (DIM)	NO
17	12.2	YES (DIM)	NO
18	15.5	NO	NO
19	12.2	NO	NO
20	13.8	YES (DIM)	NO
21	8.1	YES (DIM)	NO
22	6.4	YES (DIM)	NO
23	6.09	YES (DIM)	NO
24	6.32	YES (DIM)	NO
25	5.75	NO	NO
26	5.75	NO	NO
27	7.91	YES (DIM)	NO
28	5.86	YES (VERY DIM)	NO

Table 5. Plasma Onset Data for Unpolished 2024 Aluminum.

<u>TGT#</u>	<u>Power Density (MW/cm<sup>2</sup>)</u>	<u>Plasma Evident</u>	<u>Surface Damage</u>
29	9.10	YES	YES
30	6.66	YES	YES
31	5.97	YES	YES
32	5.40	YES	YES
33	4.04	YES	YES
34	4.49	YES	YES
35	4.09	YES (DIM)	YES
36	4.49	NO	NO
37	4.67	NO	NO
38	5.18	YES	YES
39	4.72	YES	YES
40	4.21	YES (DIM)	YES
41	4.21	YES (DIM)	YES
42	4.30	YES (DIM)	YES

Table 6. Plasma Onset Data for Polished 2024 Aluminum.

<u>TGT#</u>	<u>Power Density (MW/cm<sup>2</sup>)</u>	<u>Plasma Evident</u>
43 a	4.38	NO
43 b	5.24	NO
43 c	5.01	NO
43 d	4.89	NO
43 e	5.35	NO
43 f	5.40	NO
43 g	6.09	NO
43 h	5.06	NO
43 i	5.92	NO
43 j	5.69	NO
43 k	6.77	NO
43 l	6.26	NO
43 m	6.37	NO
43 n	5.18	NO
43 o	6.71	NO
43 p	7.40	NO
43 q	7.49	NO
43 r	7.38	NO
43 s	10.92	NO
43 t	11.13	NO
43 u	14.52	VERY DIM
43 v	13.66	NO
43 w	14.42	NO
43 x	9.66	NO
43 y	8.76	NO
43 z	16.24	NO
43 AB	18.72	NO
44	18.77	VERY DIM
72	11.10	NO

Table 6 (Cont)

<u>TGT#</u>	<u>Power Density (MW/cm<sup>2</sup>)</u>	<u>Plasma Evident</u>
73	26.71	YES (SURFACE DAMAGE EVIDENT)
74	31.30	YES
75	28.93	YES
76	18.16	VERY DIM
77	16.80	NO
78	24.68	DIM
79	21.85	DIM

Table 7. Plasma Onset Data for 0.2 Micron Si Coating on Polished 2024 Aluminum.

<u>TGT #</u>	<u>Power Density (MW/cm<sup>2</sup>)</u>	<u>Plasma Formed</u>	<u>Surface Damage</u>
82	16.29	YES	YES
88	8.09	DIM	YES
89	7.44	VERY DIM	YES

Table 8. Plasma Onset Data for 1 Micron Si Coating on Polished 2024 Aluminum.

<u>TGT #</u>	<u>Power Density (MW/cm<sup>2</sup>)</u>	<u>Plasma Formed</u>	<u>Surface Damage</u>
83	8.30	NO	NO
84	12.25	YES	YES
85	9.91	DIM	YES
86	9.81	DIM	YES
87	8.70	NO	NO

Table 9. Thermal Coupling Data for Unpolished 2024 Aluminum

<u>TGT#</u>	<u><math>\Delta T(^{\circ}C)</math></u>	<u>d(cm)</u>	<u><math>E_T(J)</math></u>	<u><math>E_D(J/cm^2)</math></u>	<u><math>P_D(MW/cm^2)</math></u>	<u><math>\alpha</math></u>
95a	.194	.170	2.025	6.73	336.4	.0118
95b	.188	.170	1.99	6.60	330.0	.0117
95c	.328	.170	2.53	8.41	420.5	.0161
104Aa	.288	.185	2.044	7.30	364.8	.0177
104Ab	.250	.185	1.79	6.39	319.6	.0175
104Ac	.185	.185	2.14	7.37	368.7	.0113
108a	.229	.190	2.12	7.85	392.5	.0134
108b	.264	.190	2.46	9.12	455.5	.0133
109	.198	.230	2.45	8.75	437.3	.0126
111a	.296	.20	2.59	9.24	462.1	.0155
111b	.234	.20	2.39	8.55	427.4	.0133
112	.290	.150	2.51	8.96	448.2	.0118

Table 10. Thermal Coupling Data for Polished  
2024 Aluminum.

<u>TGT#</u>	<u><math>\Delta T(^{\circ}C)</math></u>	<u>d(cm)</u>	<u><math>E_T(J)</math></u>	<u><math>E_D(J/cm^2)</math></u>	<u><math>P_D(MW/cm^2)</math></u>	<u><math>\alpha</math></u>
105Aa	.148	.165	1.88	6.71	335.3	.00882
105Ab	.172	.165	2.26	7.78	388.8	.00884
106a	.066	.235	2.16	7.44	372.0	.00505
106b	.120	.235	2.08	7.44	371.8	.00919
107a	.144	.190	2.23	7.67	383.7	.00865
107b	.150	.190	2.25	7.78	388.8	.00888
155	.182	.160	1.93	6.88	344.0	.01026
156	.106	.175	1.93	6.88	344.0	.00653
157a	.170	.235	2.66	8.83	441.6	.01097
157b	.078	.235	2.19	7.82	390.9	.00568
159	.194	.190	3.01	9.65	482.7	.00926

Table 11. Thermal Coupling Data for 0.2 Micron Si Coating on Polished 2024 Aluminum.

<u>TGT#</u>	<u><math>\Delta T(^{\circ}C)</math></u>	<u>d(cm)</u>	<u><math>E_T(J)</math></u>	<u><math>E_D(J/cm^2)</math></u>	<u><math>P_D(MW/cm^2)</math></u>	<u><math>\alpha</math></u>
104a	.370	.160	1.90	6.78	338.8	.0212
104b	.298	.160	2.15	7.41	370.3	.0156
105a	.234	.180	2.05	7.33	366.5	.0139
105b	.376	.180	2.49	8.58	429.0	.0191

Table 12. Thermal Coupling Data for 1 Micron Si Coating on Polished 2024 Aluminum.

<u>TGT#</u>	<u><math>\Delta T(^{\circ}C)</math></u>	<u>d(cm)</u>	<u><math>E_T(J)</math></u>	<u><math>E_D(J/cm^2)</math></u>	<u><math>P_D(MW/cm^2)</math></u>	<u><math>\alpha</math></u>
101	.162	.190	2.93	9.40	470.2	.00794
103a	.146	.150	1.85	6.60	330.1	.00804
103b	.120	.150	1.77	6.32	316.2	.00690
158a	.112	.190	3.09	9.90	495.2	.00521
158b	.134	.190	2.22	7.92	396.1	.00779

Table 13. Thermal Coupling Data for Unpolished  
304 Stainless Steel.

<u>TGT#</u>	<u><math>\Delta T(^{\circ}C)</math></u>	<u>d(cm)</u>	<u><math>E_T(J)</math></u>	<u><math>E_D(J/cm^2)</math></u>	<u><math>P_D(MW/cm^2)</math></u>	<u><math>\alpha</math></u>
115	.334	.12954	2.04	7.30	364.8	.0237
116	.306	.12954	2.12	7.57	378.7	.0209
117	.482	.12954	2.15	7.68	383.9	.0325
141a	.236	.12954	2.75	9.15	457.7	.0134
141b	.290	.12954	2.68	8.90	444.8	.0169
145a	.250	.12954	2.15	7.68	383.9	.0169
145b	.330	.12954	2.38	8.51	425.6	.0201
146	.244	.12954	2.80	9.00	450.0	.0140
147a	.412	.12954	2.80	9.00	450.0	.0237
147b	.354	.12954	2.27	8.10	404.8	.0226
148a	.300	.12954	2.57	8.54	427.0	.0182
148b	.216	.12954	2.03	7.26	363.1	.0154
149a	.176	.12954	2.21	7.89	394.3	.0116
149b	.236	.12954	2.82	9.06	453.0	.0135

Table 14. Thermal Coupling Data for Polished 304 Stainless Steel.

<u>TGT#</u>	<u><math>\Delta T(^{\circ}C)</math></u>	<u>d(cm)</u>	<u><math>E_T(J)</math></u>	<u><math>E_D(J/cm^2)</math></u>	<u><math>P_D(MW/cm^2)</math></u>	<u><math>\alpha</math></u>
119	.374	.12954	2.33	8.30	415.2	.0233
120	.504	.12954	2.25	8.03	401.3	.0325
121	.252	.12954	2.31	8.23	411.7	.0159
137	.310	.12954	1.78	6.36	317.9	.0253
138	.376	.12954	2.12	7.57	378.7	.0257
140	.184	.12954	2.82	9.06	453.0	.0105
142	.192	.12954	2.85	9.15	457.7	.0109
143	.446	.12954	2.77	9.22	461.0	.0251
144	.356	.12954	2.83	9.09	454.6	.0203
151	.194	.12954	2.01	7.16	357.9	.0140
152	.172	.12954	2.01	7.16	357.9	.0124
153	.256	.12954	2.01	7.16	357.9	.0185
154	.220	.12954	1.92	6.84	342.2	.0167

Table 15. Thermal Coupling Data for Si Coating on Polished 304 Stainless Steel.

<u>TGT#</u>	<u><math>\Delta T(^{\circ}C)</math></u>	<u>d(cm)</u>	<u><math>E_T(J)</math></u>	<u><math>E_D(J/cm^2)</math></u>	<u><math>P_D(MW/cm^2)</math></u>	<u><math>\alpha</math></u>
122	.224	.12954	2.20	7.85	392.6	.0148
123	.202	.12954	2.33	8.30	415.2	.0126
124	.263	.12954	2.42	8.65	432.6	.0158
125	.2785	.12954	2.06	7.37	368.3	.0196
150	.186	.12954	2.22	7.92	396.1	.0122

Table 16. Summary of TiC Surface Damage Evaluation shots.

<u>Target No.</u>	<u>Energy on Target</u>	<u>Power Density on Target (MW/cm )</u>
126	1.67	298.8
127	1.52	271.0
128	1.64	291.8
129	1.99	356.1
130	2.15	383.9
131	1.64	291.8
132	1.91	340.5
133	4.89	872.0
134	6.14	1096.0
135	3.20	573.3

Table 17. Measured Sample Specular Reflectivities.

<u>Material</u>	<u>Reflectivity</u>
Polished Al-2024	0.855
Polished SS-304	0.776
Si-coated SS-304	0.725
0.2 micron Si-coated Al-2024	0.594
1 micron Si-coated Al-2024	0.532
Unpolished Al-2024	0.514
TiC-coated SS-304	0.444
Unpolished SS-304	0.304

## LIST OF REFERENCES

1. Keville, M. T., and Lautrop, R. W., An Investigation of Unipolar Arcing Damage on Stainless Steel and TiC Coated Surfaces, Master of Science Thesis, Naval Postgraduate School, Monterey, California, June 1980.
2. Barker, J. H., and Rush, R. J., An Investigation of Plasma-Surface Interactions on Selected Conductors and Semi-Conductors and Insulators, Master of Science Thesis, Naval Postgraduate School, Monterey, California, December 1980.
3. Ryan, F. T., and Shedd, S. T., A Study of the Unipolar Arcing Damage Mechanism on Selected Conductors and Semi-Conductors, Master of Science Thesis, Naval Postgraduate School, Monterey, California, June 1981.
4. Hoover, T. J., An Investigation of Unipolar Arcing in Various Conductors and Metallic Glasses, Master of Science Thesis, Naval Postgraduate School, Monterey, California, September 1981.
5. Beelby, M. H., and Ulrich, H. G., A Study of the Breakdown Mechanism of AISI 304 SS, AISI 2024 Aluminum and Various Titanium Coatings, Master of Science Thesis, Naval Postgraduate School, Monterey, California, December 1981.
6. Metheny, R. M., An Investigation of Energy Coupling in Various Arc Susceptible and Resistant Conductors, Master of Science Thesis, Naval Postgraduate School, Monterey, California, June 1982.
7. Chun, M. K., and Rose, K., "Interaction of High-Intensity Laser Beams with Metals", Journal of Applied Physics, v. 41(2), p. 614-620, February 1970.
8. Ready, J. F., Industrial Applications of Lasers, p. 336-357, Academic Press, 1978.
9. Hettche, L. R., and others, "Mechanical Response and Thermal Coupling of Metallic Targets to High-Intensity 1.06- $\mu$  Laser Radiation", Journal of Applied Physics, v. 47(4), p. 1415-1421, April 1976.

10. Metz, S. A., and others, "Effect of Beam Intensity on Target Response to High-Intensity Pulsed CO<sub>2</sub> Laser Radiation", Journal of Applied Physics, v. 46(4), p. 1634-1642, April 1975.
11. Harrison, D. E., and Neighbors, J. R., Laser Effects Handbook; 3 Laser Absorption Wave Phenomena, Naval Postgraduate School, December 1975.
12. Marcus, S., Lowder, J. E., and Mooney, D. L., "Large-Spot Thermal Coupling of CO<sub>2</sub> Laser Radiation to Metallic Targets", Journal of Applied Physics, v. 47(7), p. 2966-2968, July 1976.
13. Chen, F. F., Introduction to Plasma Physics, Plenum Press, 1977.
14. Schwirzke, F., and Taylor, R. J., "Surface Damage by Sheath Effects and Unipolar Arcs", Journal of Nuclear Materials, v. 93 and 94, p. 780-784, 1980.
15. Ready, J. F., Effects of High-Power Laser Radiation, p. 67-125, Academic Press, 1971.
16. Stanley, J. K., Electrical and Magnetic Properties of Metals, American Society for Metals, 1963.
17. White, C. W., and Peercy, P.S., Laser and Electron Beam Processing of Materials, Academic Press, 1980.
18. Maher, W. E., and Hall, R. B., "Experimental Thermal Coupling of Laser Beams", Journal of Applied Physics, v. 49(4), p. 2254-2261, April 1978.
19. Schwirzke, F., Bunshah, R. F., and Taylor, R. J., The Observation of Unipolar Arc Damage on Stainless Steel and TiC Coatings on Stainless Steel, paper presented at the International Conference on Metallurgical Coatings, San Francisco, California, 6-10 April 1981.
20. McCracken, G. M., and Goodall, D. H. J., "The Role of Arcing in Producing Metal Impurities in Tokamaks", article submitted for publication in Nuclear Fusion, Culham Laboratory, U.K., October 1977.
21. Robson, A. E., and Thoneman, P. C., "An Arc Maintained on an Isolated Metal Plate Exposed to a Plasma", Institution of Electrical Engineering, v. 106, pt. A, supp. 2, p. 508-512, April 1959.

22. Miley, G. H., "Surface Effects Related to Voltage Break-down in CTR Devices", Journal of Nuclear Materials, v. 63, p. 331-336, 1976.
23. Union Carbide Electronics, KORAD Laser Systems Instruction Manual for Nd: Glass Laser, Five volumes, KORAD Department, Santa Monica, California 1969.
24. Baeri, P., and others, "A Melting Model for Pulsing-Laser Annealing of Implanted Semiconductors", Journal of Applied Physics, v. 50(2), p. 788-796, February 1979.
25. Cutler, M., Liquid Semiconductors, p. 8, Academic Press, 1977.
26. Metals Handbook, 9th ed., American Society for Metals, 1979.
27. Metals Reference Book, 5th ed., Butterworth and Co., 1978.
28. Campbell, I. E., High Temperature Technology, Wiley, 1956.
29. Guide for Material Processing by Lasers, 2nd ed., Laser Institute of America 1978.
30. Naval Research Laboratory Report 7728, Response of Materials to Laser Radiation; A Short Course, by J. T. Schriemp, p. 52, 10 July 1974.
31. Ecker, G., "Arcing Surface Phenomena", Proceedings of the International Symposium on Plasma Wall Interaction, p. 245-256, 18-22 October 1976.

INITIAL DISTRIBUTION LIST

	Copies
1. Defense Technical Information Center Cameron Station Alexandria, Virginia 22314	2
2. Library, Code 0142 Naval Postgraduate School Monterey, California 93940	2
3. Department Chairmen, Code 61 Department of Physics and Chemistry Naval Postgraduate School Monterey, California 93940	1
4. Assoc. Professor F. R. Schwirzke, Code 61Sw Department of Physics and Chemistry Naval Postgraduate School Monterey, California 93940	3
5. Assoc. Professor K. D. Challenger, Code 69 Department of Mechanical Engineering Naval Postgraduate School Monterey, California 93940	1
6. Dr. F. Weiting Code 6630 U.S. Naval Research Laboratory Washington, D.C. 20375	1
7. LCDR William F. Jenkins 826 "C" Avenue Coronado, California 92118	2
8. LCDR William R. Schmidt Code 430B Office of Naval Research 800 N. Quincy Street Arlington, VA 22217	2